LAWRENCE
LIVERMORE
NATIONAL
LABORATORY

LLNL-JRNL-452338

Global-scale P-wave tomography optimized for prediction of teleseismic and regional travel times for Middle East events: 2. Tomographic inversion

N. A. Simmons, S. C. Myers, G. Johannesson

August 31, 2010

Journal of Geophysical Research

Disclaimer

Global-scale P-wave tomography optimized for prediction of teleseismic and regional travel times for Middle East events: 2. Tomographic inversion

N.A. Simmons[1], S.C. Myers[1] & G. Johannesson[2]

[1]Atmospheric, Earth and Energy Division, Lawrence Livermore National Laboratory
[2]Systems and Decision Sciences, Lawrence Livermore National Laboratory

Corresponding author:

Nathan A. Simmons
L-046
Lawrence Livermore National Laboratory
Livermore, CA 94550
(925) 422-2473
Simmons27@llnl.gov

For submission to *Journal of Geophysical Research – Solid Earth*

Prepared by LLNL under Contract DE-AC52-07NA27344

Abstract

We construct a model of three-dimensional P-wave velocity structure in the crust and mantle that is global in extent, but with detailed upper mantle heterogeneities throughout the greater Middle East region. Fully three-dimensional ray tracing is employed to achieve accurate travel time predictions of P and P_n arrivals, necessitating the characterization of irregular and discontinuous boundaries. Therefore, we explicitly represent undulating seismic discontinuities in the crust and upper mantle within a spherical tessellation modeling framework. The tessellation-based model architecture is hierarchical in that fine node sampling is achieved by recursively subdividing a base-level tessellation. Determining the required node spacing to effectively model a given set of data is problematic, given the uneven sampling of seismic data and the differing wavelengths of actual seismic heterogeneity. To address this problem, we have developed an inversion process called *Progressive Multi-level Tessellation Inversion* (PMTI) that exploits the hierarchical nature of the tessellation-based design and allows the data to determine the level of model complexity. PMTI robustly images regional trends and allows localized details to emerge where resolution is sufficient. To demonstrate our complete modeling concept, we construct a velocity model based on teleseismic P travel time data for global events and regional P_n travel time data for events occurring throughout the Middle East. Input data are a product of the statistical procedure called *Bayesloc* that simultaneously models all components of a multi-event system including event locations, origin times and arrival times (described in the companion paper). The initial tomographic image provides a new glimpse of the complex upper mantle velocity anomalies associated with the convergence of the Arabian and Indian plates with Eurasia. More important for event monitoring, the model accurately predicts both teleseismic and regional travel times for events occurring within the Middle East region.

1. Introduction

Global-scale seismic tomography has been a major area of active research in Earth sciences since the development of the first mantle models in the late 1970's [*Sengupta and Toksöz* 1976; *Dziewonski et al.* 1977]. Over the past 3+ decades, numerous global seismic tomography models have been developed by a number of research groups and have proven to be extremely effective tools for advancing our understanding of Earth's interior [see *Romanowicz* 1991, 2003]. Recent global-scale tomographic studies have yielded solutions that are generally consistent at the longest wavelengths suggesting an imminent consensus of the 1st-order 3-D seismic velocity structure in the mantle [e.g. *Robertson and Woodhouse* 1996; *Grand et al.* 1997; *van der Hilst et al.* 1997; *Bijwaard et al.* 1998; *Widiyantoro et al.* 1998; *Ishii and Tromp* 1999; *Ritsema et al.* 1999; *Kárason and van der Hilst* 2000; *Masters et al.* 2000; *Mégnin and Romanowicz* 2000; *Gu et al.* 2001; *Zhao* 2001; *Grand* 2002; *Kennett and Gorbatov* 2004; *Trampert et al.* 2004; *Simmons et al.* 2006, 2007, 2009; *Li et al.* 2008]. However, details in global tomographic solutions differ for a number of reasons including the diversity of data types and methodologies employed. The specific approaches employed to image the Earth are often determined by the particular goals of the individual tomographic studies.

Aside from gaining a fundamental understanding of the composition and dynamics of Earth, global 3-D tomography models can be used to improve seismic event location prediction. In particular, it has been demonstrated that travel time predictions based on global tomography models can improve seismic event location accuracy [e.g. *Antolik et al.* 2001, 2003; *Ritzwoller et al.* 2003], making them potentially useful to seismic monitoring agencies. The utility of teleseismic 3-D P-wave models in assisting in event location is, of course, contingent upon the ability to detect seismic phases at a sufficient number of stations at teleseismic distances.

75 Therefore, global P-wave models, produced with teleseismic information alone, are only reliable
76 tools for locating large seismic events. Regional-scale models of upper mantle P-wave velocity
77 structure are therefore essential in locating smaller events since global-scale models generally do
78 not adequately predict regional seismic phase travel times.

79 One possible way to predict both regional and teleseismic P-wave travel times is through
80 the application of independently produced regional and teleseismic models [e.g. *Yang et al.*
81 2004]. However, hybrid combinations of independent regional and teleseismic models tend not
82 to be self-consistent since the predicted teleseismic (i.e. P) and regional (i.e. P_n) travel times
83 often conflict. At a minimum, baseline travel time shifts must be determined through the
84 calculation of travel time correction surfaces in order to reduce the 1st-order regional-teleseismic
85 travel time inconsistencies generated by the hybrid models [*Yang et al.* 2004]. To overcome
86 these issues and further advance event monitoring capabilities, we need to generate a seamless
87 model of the Earth's crust and mantle capable of self-consistently predicting regional and
88 teleseismic travel times as accurately as possible. Effectively, this requires simultaneous
89 modeling of detailed upper mantle heterogeneities to adequately predict regional phases such as
90 P_n and lower mantle structures to predict teleseismic travel times. It is also highly desirable to
91 develop a model and techniques that reduce the need for numerous travel time corrections (e.g.
92 crustal corrections, Earth's ellipticity, etc.) and/or massive travel time lookup tables.

93 In this study, we present the initial stages of the development of a seamless, global-scale
94 tomographic model suitable for advancing seismic event monitoring capabilities worldwide. The
95 established model design is based on tessellations of a spherical surface that produces an evenly
96 spaced mesh while allowing for efficient communication with model properties. Within the
97 global-scale model, we explicitly integrate multiple crustal units with pinched layers and

98 discontinuous surfaces. We also directly incorporate upper mantle transition zone topography as
99 estimated by *Lawrence and Shearer* [2008]. In addition, the model explicitly characterizes
100 Earth's asphericity in accord with the WGS84 reference ellipsoid and the expected hydrostatic
101 shape of mantle layers and the core-mantle boundary [*Nakiboglu* 1982; *Alessandrini* 1989].
102 Explicit representation of aspherical, undulating and discontinuous geologic units yields a more
103 realistic depiction of Earth's interior than traditional spherical representations; thus allowing for
104 more accurate modeling of heterogeneity at multiple scale-lengths.

105 Travel times and model sensitivities are predicted within this complex model via 3-D ray
106 tracing procedures we have designed to communicate directly with the tessellation-based model
107 architecture. We also describe a newly developed inversion technique called *Progressive Multi-*
108 *level Tessellation Inversion* (PMTI) that is well-suited for establishing regional heterogeneity
109 trends and more detailed velocity structure where justified by a given dataset. The PMTI
110 approach is demonstrated through synthetic simulations and applied to a compiled set of *P* and
111 P_n data designed to provide strong constraints on velocity structures throughout the greater
112 Middle East region. The seismic events used in this study are located with a statistical multiple-
113 event locator called *Bayesloc* [*Myers et al.* 2007; 2009] that simultaneously models all event
114 locations, origin times, arrival times and phase labels to produce an extremely consistent dataset
115 (see the companion paper in this issue by *Myers et al.*). Our result is a global-scale model of P-
116 wave velocity structure based upon *P* and P_n travel times from >4,000 Middle East events and
117 >1,000 globally distributed seismic events.
118

2. Model Representation

Our model parameterization is based on triangular tessellations of a spherical surface. Spherical tessellation parameterizations have been employed for multiple geophysical applications including mantle convection simulations [*Baumgardner and Frederickson* 1985], magnetic field modeling [*Constable et al.* 1993; *Stockmann et al.* 2009], and the basis for representation of Earth's seismic velocity structure [e.g. *Wang and Dahlen* 1995; *Chiao and Kuo* 2001; *Ishii and Dziewonski* 2002; *Antolik et al.* 2003; *Sambridge and Faletič* 2003; *Ballard et al.* 2009; *Gung et al.* 2009; *Myers et al.* 2010a]. The primary purpose for employing spherical tessellations is to generate a mesh of nearly evenly spaced nodes (or knots), therefore preventing the polar distortion effects of a latitude-longitude grid. Building a spherical tessellation mesh involves recursive subdivision of triangular facets of an initial polyhedron (in our case, an icosahedron) into smaller sub-triangles whose vertices are projected onto a unit sphere (Figure 1). Each sub-division of a triangular facet ('*parent*') produces 4 triangular facets ('*daughters*') and thus increases the number of nearly evenly spaced vertices. We refer to each tessellation recursion as a '*Level*' starting with the initial object (Level 1; Figure 1) up to Level *N*, where *N* is some maximum recursion level. For example, a Level 7 recursion results in node spacing of approximately 1° when an icosahedron is used as the initial object.

Although the tessellation meshes represent simple sphere-like surfaces, they form the basis of an aspherical Earth representation in this study. We define a set of geocentric unit vectors connecting the origin to each of the vertices defined by a tessellation mesh as $V = \left[\hat{\mathbf{v}}_1, \hat{\mathbf{v}}_2, \ldots, \hat{\mathbf{v}}_n\right]$ where n is the total number of vertices at any given level. In order to define a surface in the model space, radii are assigned to each of the vertices forming a set of nodes (or '*nodeset*') written as $N_j = \left[r_{j,1}\hat{\mathbf{v}}_1, r_{j,2}\hat{\mathbf{v}}_2, \ldots, r_{j,n}\hat{\mathbf{v}}_n\right]$ where j is the nodeset identifier. Therefore, the

142 oblateness of the Earth as well as higher order surface irregularities are explicitly built into the
143 model by simply defining an appropriate set of radii for a given set of tessellated vertices (V).
144 Pure seismic discontinuities are treated by defining two nodesets (*a* and *b*) at the same radii
145 ($N_a = N_b$) but attributing different material properties to each set. As an example, the
146 Mohorovičić discontinuity (Moho) is represented by two nodesets (N_{moho+} and N_{moho-}) with
147 lower crustal velocities associated to N_{moho+} and upper mantle velocities assigned to N_{moho-}.
148 Multiple nodesets may converge to the same radius in cases where geologic units pinch out (such
149 as sedimentary layers).

150 The major benefit of the tessellation-based model design is the nearly evenly spaced set
151 of vertices it provides. However, the set of vertices are not located at even increments in any
152 traditional coordinate system (such as spherical latitude-longitude grids), thus requiring a more
153 sophisticated indexing approach to efficiently extract model properties at any arbitrary point.
154 Indexing the parent-daughter triangle relationships during tessellation mesh design, allows for
155 efficient communication with the model through a hierarchical version of the triangle search
156 method described in *Lawson* [1984]. The interpolation approach described herein is described
157 by *Ballard et al.* [2009], but reiterated for clarity of further discussion.

158 Consider a single triangle, T_{abc}, with vertices $[\hat{\mathbf{v}}_a, \hat{\mathbf{v}}_b, \hat{\mathbf{v}}_c]$ arranged in counter-clockwise
159 order and unit vector in the direction of a point of interest ($\hat{\mathbf{p}}$) (Figure 2). It can then be
160 determined that $\hat{\mathbf{p}}$ is within the triangular wedge defined by $[\hat{\mathbf{v}}_a, \hat{\mathbf{v}}_b, \hat{\mathbf{v}}_c]$ if these three scalar
161 triple products are nonnegative:

162
$$\begin{aligned} w_a &= (\hat{\mathbf{v}}_b \times \hat{\mathbf{v}}_c) \cdot \hat{\mathbf{p}} \\ w_b &= (\hat{\mathbf{v}}_c \times \hat{\mathbf{v}}_a) \cdot \hat{\mathbf{p}} \\ w_c &= (\hat{\mathbf{v}}_a \times \hat{\mathbf{v}}_b) \cdot \hat{\mathbf{p}} \end{aligned} \qquad (1)$$

These quantities (w_a, w_b, w_c) are computed for the triangles defined in the Level 1 tessellation (icosahedron consisting of 20 triangular faces) and the parent triangle enclosing the point of interest is determined. The four associated daughter triangles in the Level 2 tessellation are subsequently searched and the process is repeated until the maximum tessellation level is reached. A maximum of 20+4(N-1) triangles are searched, where N represents the highest tessellation level. For example, if we were interested in finding the triangle that encompasses a point at tessellation Level 7 (81,920 triangles; ~1° vertex spacing), a maximum of 20+4(7-1)=44 triangles and a minimum of 7 (1 triangle per level) need to be searched.

Conveniently, the values w_a, w_b and w_c correspond to the barycentric (or areal) coordinates of the triangle T_{abc} when normalized by their sum. Thus, w_a, w_b and w_c are suitable lateral interpolation coefficients for the model properties at nodes defined along the vertices $\hat{\mathbf{v}}_a$, $\hat{\mathbf{v}}_b$ and $\hat{\mathbf{v}}_c$, respectively. With irregular surfaces directly incorporated into the model design, radial interpolation is not as trivial as with regularly spaced layers and fixed layer thicknesses. In order to determine the radial interpolation weights for any arbitrary point-of-interest (POI), a radial profile is created through lateral interpolation of radii defined along the vertices of the highest level triangle ($[\hat{\mathbf{v}}_a, \hat{\mathbf{v}}_b, \hat{\mathbf{v}}_c]$, Figure 2). Simple linear interpolation is then performed in the radial direction based on the distances of the POI to the surrounding interpolated nodeset radii. Although the efficient interpolation procedure may seem inconsequential for building an Earth model, this rapid communication with the model is essential for integration into a routine event monitoring system. Moreover, the hierarchical triangle search inherently produces lateral interpolation weights for every recursion level, thus providing an efficient means for calculating sensitivity kernels at any (or all) recursion level(s).

185

186 **3. Mixed-determined Tomographic Inversion and Parameterization Schemes**

187 Travel time tomography involves developing a set of linear equations relating

188 perturbations of seismic slowness to travel time observations in the form:

189 $$\mathbf{Ax} = \mathbf{b} \qquad (2)$$

190 In Equation 2, **A** is a matrix of model sensitivities, **b** is a collection of observations (e.g. travel

191 time residuals), and **x** is a vector of seismic slowness perturbations to be determined through

192 some inversion process. The inversion procedure is often unstable due to the mixed-determined

193 nature of typical tomographic systems. This requires some form of regularization such as

194 damping (**D**) and/or smoothing (**S**) operators to stabilize the solution:

195 $$\begin{bmatrix} \mathbf{A} \\ w_d\mathbf{D} \\ w_s\mathbf{S} \end{bmatrix}\mathbf{x} = \begin{bmatrix} \mathbf{b} \\ \mathbf{0} \\ \mathbf{0} \end{bmatrix} \qquad (3)$$

196 where w_d and w_s are damping and smoothing weights, respectively. For severely ill-posed

197 problems, determining the optimum regularization operators and corresponding weights is

198 difficult and often speculative. Mixing teleseismic and clusters of regional seismic information

199 generates a global tomographic system that is especially ill-posed given the tremendous

200 variability of data sampling. We can attempt to overcome the instability of the tomographic

201 system by limiting the number of free parameters by coarsely parameterizing the Earth. This

202 translates to using a low-level tessellation grid (in our case) or solving for relatively low-degree

203 harmonic components of the velocity field in tomographic systems built on a global parameter

204 basis. However, if the parameterization is uniformly coarse, details are inherently suppressed in

205 regions where data coverage is dense enough to image small-scale features.

206 An increasingly common parameterization strategy is to establish an irregular grid of
207 nodes/cells based on some criteria prior to inversion [e.g. *Inoue et al.* 1990; *Bijwaard et al.*
208 1998; *Kárason and van der Hilst* 2000; *Spakman and Bijwaard* 2001; *Boschi* 2006; *Li et al.*
209 2008]. The purpose in developing irregular grids is to address the variable data
210 coverage/resolution and, in addition, reduce the size of the tomographic system. The *a priori*
211 determination of variable parameter density is often based on data density (often quantified by
212 hit count) since it is reasonable to assume that resolution increases where data are plentiful.
213 However, hit count is not always an ideal indicator of resolvability, particularly when
214 considering scattered clusters of seismic rays traveling in a near-uniform direction. An irregular
215 gridding approach based on some estimate of the local resolving lengths is another possibility,
216 but an accurate measure of resolvability is difficult to determine for large tomographic systems
217 [e.g. *Nolet and Montelli* 2005].
218 Other parameterization strategies are dynamically adaptive such that meshes/cells evolve
219 during an inversion [e.g. *Sambridge and Faletič* 2003]. Opposed to building an irregular grid
220 prior to inversion, dynamically adaptive parameterization approaches require some criteria to add
221 or remove model parameters. Model-based node placement criteria (amplitude changes or
222 velocity gradients established in a prior step) may be employed for adding or removing model
223 nodes; but deciding upon the optimal criteria is a subjective process. The subjectivity of
224 parameter refinement criteria may be avoided through a stochastic search for parameter
225 definitions and seismic models in a Bayesian framework [*Bodin et al.* 2009]. Full stochastic
226 modeling approaches are more complete than deterministic modeling and are computationally
227 feasible for regional-scale and/or 2-D problems [e.g. *Pasyanos et al.* 2006; *Bodin et al.* 2009].
228 For the 3-D global problem with comprehensive representations of complex Earth structure and

229 massive amounts of data, stochastic approaches are computationally intensive. Moreover,
230 stochastic modeling would require prior constraints on anomaly correlation length, which is
231 tantamount to model smoothing.

232 To account for variable spatial resolutions and to avoid designing an irregular model grid,
233 tomographic inversion may be performed on regular coarse and fine grids simultaneously [e.g.
234 *Zhou* 1996, 2004; *Chiao and Kuo* 2001; *Chiao and Liang* 2003; *Gung et al.* 2009]. Overlapping
235 grids may be considered explicitly within an inversion [*Zhou* 1996, 2004] or implied through a
236 wavelet-based multi-resolution representation [*Chiao and Kuo* 2001; *Chiao and Liang* 2003;
237 *Gung et al.* 2009]. The common premise behind these multi-resolution approaches is that high-
238 resolution solutions can be expressed as perturbations to a low-resolution model. Thus a multi-
239 resolution model can be decomposed into hierarchical model components with differing scale
240 lengths as determined by the number of recursive parameter grid subdivisions. The multi-
241 resolution model decomposition is analogous to a spherical harmonic decomposition, but with
242 local parameter bases that inhibit artifacts in poorly sampled regions [*Boschi and Dziewonski*
243 1999]. Multi-resolution tomography representations [e.g. *Zhou* 1996; *Chiao and Kuo* 2001]
244 provide intrinsic regularization since the parameters associated with the coarsely defined grids
245 generally carry heavier weights than the parameters associated with the base-level grid
246 subdivisions. Therefore, the subjectivity of choosing global and/or local regularization operators
247 and weights is mitigated. In the following section, we describe our simplified inversion
248 approach that has many of the same desirable properties as the wavelet-based approach including
249 natural regularization without the requirement for an irregular grid design.
250

4. Progressive Multi-level Tessellation Inversion (PMTI)

The tomographic procedure developed within this study, *Progressive Multi-level Tessellation Inversion* (PMTI), is designed with the same underlying philosophy as the wavelet and multi-grid approaches described above [e.g. *Chiao and Kuo* 2001; *Zhou* 1996]. Specifically, the PMTI technique circumvents the need for predefining variable resolution scales through the hierarchical expression of higher resolution solutions as perturbations to lower resolution models. The most notable difference of PMTI from the wavelet and multi-grid approaches is that model components are found *progressively* through inversions of tomographic systems built upon successively finer parameterizations defined by a hierarchy of tessellation grids. Therefore, multiple parameter grids with different node densities are not considered simultaneously and wavelet transforms are unnecessary. Each successive model component is added to the previous solution to form a total model field. As with the wavelet and multi-grid approaches, the data drive the resulting variable resolution scales and finer detail structures emerge from the regional trends only where it is necessary to explain the given set of observations. The PMTI process is described at a high level by the algorithm:

$$
\begin{aligned}
&\mathbf{x}_1 = \mathbf{A}_1^{-1}\mathbf{b} \\
&\mathbf{b}_1 = \mathbf{b} - \mathbf{A}_1\mathbf{x}_1 \\
&\textit{for } i = 2 \ldots N \\
&\qquad \mathbf{x}_i = \mathbf{x}_{i-1}^{*} + \mathbf{A}_i^{-1}\mathbf{b}_{i-1} \\
&\qquad \mathbf{b}_i = \mathbf{b} - \mathbf{A}_i\mathbf{x}_i \\
&\textit{end}
\end{aligned}
\qquad (4)
$$

In this algorithm, the subscripts denote the recursion level (or resolution level) and the superscript "-1" refers to matrix inversion. As in the basic (simplified) tomographic system of equations (Equation 2), the variables **A**, **x** and **b** are the sensitivity kernels, slowness perturbation models, and residual travel time data vectors, respectively. In the case of our tessellation-based

model, $\mathbf{A}_1$ corresponds to sensitivity kernels for the starting object (i.e. the 1st-level spherical tessellation) and $\mathbf{A}_2$ corresponds to sensitivities to the model nodes defined by the 2nd-level tessellation (see Figure 1).

Beginning with the initial travel time residuals ($\mathbf{b}$) and sensitivity kernels defined at the lowest resolution level ($\mathbf{A}_1$), an initial slowness perturbation model ($\mathbf{x}_1$) is determined through an inversion process. The initial travel time residuals are subsequently reduced by the residuals predicted by the lowest-resolution solution to produce a new data vector, $\mathbf{b}_1$. An inversion is then performed on the basis of sensitivity kernels defined at the next resolution level ($\mathbf{A}_2$) and the reduced data vector ($\mathbf{b}_1$). The total slowness perturbation model ($\mathbf{x}_2$) accumulates by summing the interpolated model from the previous step ($\mathbf{x}_1^*$) and the higher resolution solution based on the remaining travel time signals ($\mathbf{A}_2^{-1}\mathbf{b}_1$). All subsequent inversions operate on data vectors reduced by the previous solution ($\mathbf{b}_{i-1}$) to produce slowness perturbations relative to the previous model. Therefore, if a low-resolution solution accounts for all of the travel time signal, the total slowness model ceases to accumulate additional slowness perturbations.

To develop the sensitivity kernels at each tessellation level, one could simply redistribute sensitivity weights from nodes defined by the highest tessellation level to a set of nodes defined at a lower level (i.e. collapse the linear system by combining node sensitivities). This collapsing procedure would nonetheless require defining sensitivity kernels at the highest tessellation level considered. We find it convenient to define kernels for each level simultaneously since the hierarchical triangle searching algorithm determines node interpolation weights at each of the tessellation levels automatically (see the previous section).

292 To evaluate the behavior of the PMTI approach, we devised a simple 1-D synthetic test
293 case that mimics an ill-posed and mixed determined tomographic problem (Figure 3). We placed
294 6 equally spaced nodes along a line to represent the 1st recursion level (Figure 3, top). Points
295 were then placed at the midpoints between the 1st level points to construct the 2nd recursion level
296 set of nodes. This recursion was repeated once again to give a total of 21 node points and a total
297 of 3 tessellation levels. Seismic velocities were assigned to the nodes to imitate the uppermost
298 mantle P-wave velocity structure, transitioning from a platform/shield environment (with fast,
299 long-wavelength velocity structure) to a tectonically active environment (with lower overall
300 velocity and shorter wavelength heterogeneities) (Figure 3, middle).

301 For a single test, we randomly generated 100 ray paths along the line of points while
302 forcing most of the paths to be within the tectonically active region (Figure 3, bottom). Travel
303 times were computed along each of the paths and 30% (RMS) random noise was incorporated.
304 Inversions were performed at each recursion level individually (simple inversion) and with the
305 PMTI approach for comparison (Figure 4). Simple damping was used to regulate the systems
306 and the damping weight was independently optimized for each inversion style to produce models
307 with the lowest level of RMS misfit to the known solution. For this particular path/noise
308 configuration, the PMTI approach more effectively reproduces the known solution (Figure 4).
309 Within the stable platform/shield environment, a simple inversion fails to reproduce the known
310 structure, particularly if the Level 3 nodes are active in the inversion. However, the PMTI
311 approach produces a smooth, long-wavelength trend in the poorly sampled platform region while
312 also reproducing the shorter wavelength features within the tectonically-active environment.
313 This test offers some insight into the value of the PMTI approach, but it is only a single
314 realization of path/noise configuration.

For a more comprehensive comparison of inversion approaches (simple versus PMTI), we chose to test a number of random path configurations, noise levels and damping weights. For a chosen damping weight and noise level, we randomly generated 100 paths (producing the general sampling configuration discussed above) 100 times and added random noise. For each realization of paths and noise, we performed both inversion procedures and computed the RMS misfit to the known solution. This process was repeated for a discrete set of damping weights and RMS noise levels ranging from 0 to 50%. Based on these tests, we find that the PMTI approach most often produces solutions that more closely match the known velocity model, regardless of the noise level and damping weight (Figure 5). As demonstrated in Figure 5, the optimal range of damping weights tends to be larger for the PMTI procedure owing to the intrinsic regularization. This is a valuable property of the approach since the actual solution is unknown in real cases.

We also devised a 3-D synthetic test bed to further explore the intricacies of the PMTI imaging procedure. The synthetic model domain consists of 3 triangular depth slices with nodes defined by a tessellation procedure up to the Level 5 (Figure 6). Again, we chose to mimic complex, sub-crustal P-wave velocity structure with two dominating characteristic wavelengths. Specifically, the synthetic model consists of a long-wavelength regional velocity trend with short-wavelength details embedded within the center of model domain (Figure 6, left). The velocities of the triangular depth slices above and below the center slice (shown in Figure 6) were set to a constant value to simplify the tests. The chosen ray path configuration consisted of clusters of regional phases (sub-lateral travel direction) and teleseismic paths (near vertical travel direction). The ray path density is highly heterogeneous and designed to imitate a realistic shallow mantle imaging problem. That is, some regions are well-covered with ray paths

338 traveling in many different directions, whereas other regions are sampled by only a single cluster
339 of teleseismic or regional phases. Random noise was also added to the synthetic travel time
340 observations.

341 Similar to the 1-D synthetic test case, inversions were performed directly (simple least-
342 squares at the highest tessellation level) and with the PMTI procedure for comparison. A
343 representative solution from a single realization (paths shown in Figure 6 and 20% RMS noise
344 added) is shown in Figure 7. For the simple (or direct) inversion, we incorporated simple
345 damping and smoothing operators independently and optimized the regularization weights to
346 find the solutions closest to the known solution (based on RMS model misfit). With damping
347 alone, detailed structures emerge where there are a large number of crossing paths (Figure 7;
348 SIMPLE damping). However, instead of recovering the long-wavelength regional trend, isolated
349 velocity structures are generated without a smooth transition through unresolved regions. In
350 regions with only near-vertical paths (~teleseismic phases), circular velocity structures are
351 generated since there is no sensitivity to surrounding nodes. In regions with only bundles of sub-
352 horizontal paths (~regional phases), linear velocity anomalies are evident. Such isolated velocity
353 blobs and streaks are undesirable since they may result in geological misinterpretations and also
354 pose serious problems when computing travel times with 3-D ray paths. Alternatively, simple
355 inversion with a first-order smoothing operator (with an optimum weight) recovers the long-
356 wavelength regional trend, but fails to recover fine details where information is sufficient (Figure
357 7; SIMPLE smoothing). This smooth solution is also undesirable since we would prefer to take
358 full advantage of the resolvability of dense data packets.

359 With the PMTI approach, the long-wavelength velocity structure is established with the
360 first inversion based on nodes defined by the first level tessellation (Figure 7; PMTI Level 1).

361 Note that only simple damping is used as regularization. The Levels 2-4 PMTI solutions adjust
362 the model only slightly, relative to the Level 1 solution. The minor model variation provided by
363 these intermediate steps is due to the synthetic velocity model design with only two dominating
364 characteristic wavelengths. In the final PMTI stage (Level 5 inversion), detailed structures
365 emerge from the underlying long-wavelength velocity trend (Figure 7; PMTI Level 5). The
366 detailed anomalies are most refined where data coverage is dense and ray path travel directions
367 are diverse. Our tests reveal that, similar to the 1-D synthetic example, the PMTI solution is less
368 dependent on the choice of damping weight than a simple direct inversion. Moreover, a direct
369 (simple) inversion requires both smoothing and damping regularization with strictly optimized
370 regularization weights to achieve a result similar to the PMTI solution shown in Figure 7.

371 The *Progressive Multi-level Tessellation Inversion* (PMTI) approach has important
372 advantages over other inversion techniques, especially when considering extreme spatial
373 resolvability variations. If the travel time observations cannot be explained by a long-
374 wavelength velocity trend in a particular region, detailed anomalies emerge from the background
375 velocity model. Therefore, the 'resolution level' is predicated by the data without any user
376 intervention. Dynamic mesh refinement (or adaptive meshing) is one such method of
377 intervention whereby the addition or subtraction of model parameters occurs based on some
378 user-defined criteria, thus generating an irregular grid. Aside from the additional complexity of
379 establishing and communicating with a model based on an irregular grid, our synthetic example
380 demonstrates other potential pitfalls of a dynamic/adaptive mesh refinement approach (Figure 7).
381 For example, if we chose to refine the mesh from one inversion step to the next based on model
382 movement, the imaging process would cease after the inversion based on the nodes defined by
383 the Level 2 triangular tessellation (see Figure 7). This cessation could be prevented through

384 knowledge of the data density (e.g. hit count criteria). However, hit count does not necessarily
385 reflect resolvability since ray paths are commonly bundled providing limited additional
386 constraints on lateral velocity variations. For ultra-high resolution modeling with a global basis
387 (<0.5° node spacing), adaptive meshing may be required to limit the size of the tomographic
388 systems of equations. For our initial global model design, we find that irregular meshing is
389 unnecessary.

390 Similar to the multi-grid and wavelet-based approaches [e.g. *Zhou* 1996; *Chiao and Kuo*
391 2001], the PMTI technique adapts to the variable lateral resolvability of a given dataset while
392 reducing the subjectivity of regularization operators and weighting. Unlike other multi-
393 resolution approaches, PMTI progressively solves for detailed structure at discrete inversion
394 steps. This progressive-style approach is relatively simple and provides the flexibility to easily
395 perform operations while the tomographic model evolves from a low- to a high-resolution
396 solution. We do not take advantage of this particular benefit in our initial modeling procedures
397 (described below); however, it is potentially a very beneficial property for future modeling. For
398 example, we may choose to increase depth resolution (with lateral resolution) by simply adding
399 model layers before proceeding to higher tessellation levels. Furthermore, outlier data could be
400 more easily identified from the population of data after performing low-resolution inversions,
401 and subsequently removed before continuing the inversion process. Additionally, 3-D ray paths
402 may be updated during the resolution progression to account for the path-velocity dependence.

403

5. Global 3-D Tomography with Middle East Emphasis

5.1. Travel Time Data and Event Locations

We compiled a Middle East-centric set of teleseismic *P* and regional P_n travel time measurements from a subset of our local database at Lawrence Livermore National Laboratory [*Ruppert et al.* 2005] and the publicly available Engdahl-van der Hilst-Buland (EHB) catalog [*Engdahl et al.* 1998]. The data selection criteria were: 1) all available *P* and P_n travel time measurements from seismic events occurring within the greater Middle East region, and 2) teleseismic *P* measurements from globally distributed events with the largest number of recordings within 5° lateral bins and 7 depth bins from the surface to 700 km depth. In total, we consider 5,401 events (~4,000 within the Middle East) recorded at approximately 4,500 seismic stations around the globe. The data consist of ~800,000 *P* arrivals from globally distributed events and stations, and ~42,000 P_n arrivals to stations within the Middle East (Figure 8). Although the compiled dataset is global in extent, more than 60% of the data are from events occurring within the Middle East and/or arrivals to one of the 600+ seismic stations within the region. Ray path hitcount calculations reveal that most of the shallow upper mantle in the Middle East region is sampled by more than 1,000 *P* and 100 P_n paths providing excellent constraints on detailed velocity structure (Figure 9).

One of the major issues in seismic tomography is knowledge of the precise location of events from which the travel time residual data are derived. It may be argued that, event location accuracy becomes less important with increasing amounts of data since interpretable anomalies may emerge from the background velocity field. However, systematic location errors may result in the inability to resolve true Earth structure, regardless of the amount of data considered. Thoroughly addressing this issue is crucial since the purpose of this work is to design a global-

427 scale model that predicts travel times for the most accurate prediction of future seismic event
428 locations. We therefore adapted a multi-event location algorithm, initially designed to
429 simultaneously locate event clusters, to handle a global distribution of seismic events [*Myers et*
430 *al.* 2007, 2009]. The algorithm, called *Bayesloc* is briefly described here for completeness. A
431 thorough description can be found in a companion paper in this issue [*Myers et al.* 2010b].
432 *Bayesloc* is a multi-event location algorithm that operates within a hierarchical Bayesian
433 statistical framework. The process entails generating numerous realizations of event
434 hypocenters, origin times, phase labels, and travel time curves using a Markov Chain Monte
435 Carlo (MCMC) sampling scheme. Using prior statistical models, the process allows for
436 complete statistical characterization of the multi-event problem and thus develops a joint
437 posterior distribution of all elements involved. The *Bayesloc* algorithm simultaneously
438 determines event location probability regions, identifies likely outlier arrival time data
439 (inconsistent with the total population), re-labels misidentified seismic phases, and adjusts travel
440 times based on statistically likelihood. The net result of the procedure is a set of event locations
441 and travel times such that the spread of the travel time residuals relative to a 1-D velocity model
442 is minimal (Figure 10).
443 Numerous seismic phases, for the aforementioned set of events, were included within the
444 *Bayesloc* location procedure. However, we chose to consider only globally distributed *P* arrivals
445 and P_n arrivals in the Middle East region for tomographic imaging. The average event locations
446 and origin times from the joint posterior probability distribution were used to form the set of
447 travel time data for the tomographic problem. The effect of the relocation procedure is
448 demonstrated in terms of the residual travel time spread relative to the 1-D AK135 [*Kennett et al.*
449 1995] global P-wave velocity model (Figure 10). In terms of data variance, the apparent travel

450 time residual signal of the raw data (based on the original event locations) is ~12 times larger
451 than the signal based on the *Bayesloc* event locations. This suggests that a tremendous amount
452 of the apparent signal associated with the raw event locations is not due to 3-D velocity structure,
453 but rather hypocenter mis-location, mis-identified seismic phases and arrival time pick errors.
454 The total signal reduction signifies the improved data consistency that *Bayesloc* provides,
455 but another important aspect is the shift of the mean from a positive 0.44 seconds to a negative
456 0.53 seconds. This mean shift and the residual trend with distance (see Figure 10) have
457 tremendous implications on the absolute velocity structure needed to explain the data.
458 Hypocenter locations based on single-event location procedures often do not recover such trends;
459 particularly when assuming a location such that the residual travel times are zero-mean.
460
461 **5.2. Hybrid Starting Model**
462 A starting 3-D P-wave velocity model was designed by combining components of
463 existing models of the crust and mantle to form a single hybrid model. The hybrid model was
464 built within the tessellation-based node architecture described in previous sections. Components
465 of the crust below Eurasia and northern Africa (between 0° and 90°N latitude and 20°W to 75°E
466 longitude) were taken from a modified version of the compilation of *Pasyanos et al.* [2004] and
467 *Steck et al.* [2004]. Modification of the Eurasia/Africa crustal model is based on the regional
468 travel time tomography described in *Myers et al.* [2010a]. Outside of Eurasia and North Africa,
469 we employed the crustal model of *Bassin et al.* [2000] (Crust 2.0). The crust consists of 7 layers
470 including water, 3 sediment layers (with ice layers), and 3 crystalline crustal units (upper, middle
471 and lower). These layers were built into the tessellation-based model framework with 14
472 nodesets describing the top and bottom of each of the discontinuous layers. We defined the

crustal components (velocities and depths) at discrete points along vertices corresponding to tessellation Level 7 (~1° node spacing). All model node points were projected in the radial direction to conform to the WGS84 reference ellipsoid.

Sub-crustal (shallowest upper mantle) P-wave velocity structure was taken from the Regional Seismic Travel Time (RSTT) model [*Myers et al.* 2010a]. The shallow upper mantle velocity structure in the RSTT model is represented by the mantle velocity at the Moho (often referred to as P_n velocity) and a depth-dependent velocity gradient. The RSTT mantle velocity and mantle gradient terms were interpolated to a fully three-dimensional velocity field immediately below the Moho to a depth of 115 km. Similar to the representation of the crust, the shallowest upper mantle P-wave velocity and boundaries were defined at points along the Level 7 tessellation vertices (~1° node spacing).

The remainder of the mantle velocity structure (115 km depth to the core-mantle boundary) was based on the GyPSuM Earth model [*Simmons et al.* 2010 (in press)]. GyPSuM is a 3-D model of mantle S-wave speed, P-wave speed and density developed through simultaneous inversion of seismic and geodynamic constraints. The GyPSuM model represents the next major phase of a sequence of joint global modeling efforts fully described in *Simmons et al.* [2006, 2007, and 2009]. The shear wave data consist of waveform-correlation-based travel time measurements for numerous teleseismic phases including *S*, *sS*, *ScS*, *SKS*, and numerous surface- and core-reflected multiples [*Grand* 2002; *Simmons et al.* 2006]. The geodynamic information consists of the global free-air gravity field, dynamic surface topography, tectonic plate motions, and the excess core-mantle boundary (CMB) ellipticity. These geodynamic observations are linearly related to internal density loads in the Earth through viscous flow sensitivity kernels; and density is coupled to velocity structure via mineral physics parameters.

For the purposes of the current study, the most important improvement of GyPSuM over the past global joint models [e.g. *Simmons et al.* 2006, 2007, 2009] is the addition of globally distributed teleseismic P-wave arrivals from the work of *Engdahl et al.* [1998] and *Antolik et al.* [2003]. Wave speeds and density are coupled together with relative heterogeneity ratios constrained by mineral physics parameters that describe the effect of temperature variations on mantle material. Non-thermal effects are gradually introduced producing a mantle heterogeneity model that is most consistent with thermal variations and model fields (S/P wave speeds and density) that most resemble one another. Thus, several forms of data (seismic, geodynamic and mineral physics) control the outcome of each of the modeled properties in an explicit, non-linear joint inversion process.

Upper mantle P-wave velocity structure from the GyPSuM Earth model was integrated into the tessellation-based model architecture. Upper mantle velocities were defined along vertices corresponding to tessellation Level 7 (~1° spacing) at discrete depths (radii) with average depth spacing of ~40 km. For the initial model design, transition zone boundary depths were fixed according to PREM [Dziewonski and Anderson 1981]. Similar to the upper mantle, lower mantle P-wave velocity structure from the GyPSuM model was incorporated into the tessellation-based model design. However, we chose to define model nodes along vertices corresponding to the Level 6 tessellation (~2° spacing) to limit the number of model parameters. The lower mantle velocity field is represented by 25 nodesets (layers) with an average depth spacing of ~90 km.

In summary, the crust and upper mantle velocity model is represented by 33 nodesets (layers) with a lateral spacing of ~1° (Level 7 tessellation) and the lower mantle is represented by 25 nodesets (layers) with a lateral spacing of ~2° (Level 6 tessellation). In total, the crust and

519 mantle P-wave velocity structure is defined at ~1.6 million points (1.35 million points in the
520 crust and upper mantle; 250,000 points in the lower mantle). This hybrid starting model will be
521 referred to as 'RSTT+GyPSuM' in further discussions.
522
523 **5.3. Travel Time Calculations and Sensitivity Definitions**
524 In order to accurately predict travel times and model space sensitivities in complex 3-D
525 media, we have adapted a 3-D ray tracing procedure specifically tailored to communicate with
526 the aforementioned tessellation-based model design. The general approach we have taken is
527 based on the techniques originally conceived by *Zhao et al.* [1992] to model direct arrivals
528 within a subduction zone and extended to teleseismic phases by *Zhao and Lei* [2004]. The
529 procedure combines pseudo-bending in continuous media [*Um and Thurber* 1987] while
530 simultaneously satisfying Snell's Law at discontinuous interfaces through an iterative process.
531 The bending/interface iterations continue until the minimum-time-path is found; or the process is
532 terminated when travel time reduction is nominal from one step to the next.
533 One major shortcoming of this general approach is the inability to find global minimum
534 travel times and paths for complex regional phases such as P_n. We have therefore adapted the
535 procedure to find such global minima by considering multiple starting ray path configurations.
536 A similar adaptation has recently been developed by *Ballard et al.* [2009] where the
537 computational process was designed within a distributed computing environment. *Ballard et al.*
538 [2009] demonstrated the ability to dramatically improve the efficiency of the technique thus
539 providing support for the implementation of the general approach for routine seismic event
540 location.

In our specific approach, we initially create several crude 3-D ray path estimates based on an imposed set of rules for a given source-receiver configuration (Figure 11). Each of the initial paths is perturbed with a limited set of pseudo-bending iterations and discontinuity piercing point adjustments as described in *Zhao et al.* [1992]. Rather than performing ray path adjustment iterations until convergence, we cull out paths that provide travel times within some tolerance of the minimum time achieved by the full set of perturbed paths (we chose a 1 second tolerance). Ray path adjustment iterations are then performed on the remaining paths until the minimum travel time is attained. The paths that generate the minimum time within a secondary time tolerance (we chose 0.2 seconds) are accepted and used in the development of model space sensitivity kernels. For example, near the upper mantle transition zone crossover distance range (~18° distance for a surface event), ray paths traveling through the shallow upper mantle and below transition zone discontinuities are accepted if they satisfy the minimum time tolerance criterion. By accepting all paths that produce near-minimum travel times, we directly address the multi-pathing problem. Additionally, model sensitivity may be distributed over a wide depth range as opposed to two (or more) distinct geological units in a pure multi-pathing scenario (see the example in Figure 11). Thus, the issue of interdependence of velocity structure and ray path is mitigated. This procedure is similar to the "fat ray" approach described in *Husen and Kissling* [2001]; however, our primary concern is with distinct multi-paths rather than perfectly representing a Fresnel volume. Our model space sensitivity definition may also be considered a compromise between linear 3-D ray paths and finite frequency sensitivity [*Dahlen et al.* 2000]; albeit our approach is a less comprehensive/formal description of seismic sensitivity.

Three-dimensional ray paths were computed for each of the data on the basis of the hybrid 3-D velocity model (RSTT+GyPSuM). The individual RSTT and GyPSuM models are

564 based on regional and teleseismic travel times, respectively. However, the hybrid model fails to
565 predict P_n and P arrivals better than the 1-D AK135 model (Figure 10). Based on the overall
566 residual travel time statistics, travel time predictions using on the hybrid velocity model (with 3-
567 D ray paths) are actually less consistent with the data than AK135 (with 1-D ray paths). There
568 are a number of potential causes for this degradation including the different crustal models used
569 for each (RSTT and GyPSuM), and the different forward theories used in their development.
570 Particularly, the GyPSuM model assumes Crust 5.1 [*Mooney et al.* 1998] and the forward model
571 was based on 1-D ray paths. RSTT, on the other hand, assumes the same crustal structure that is
572 built into the hybrid RSTT+GyPSuM model (see the previous section and *Myers et al.* [2010a]).
573 The forward model design used for RSTT is based on ray paths constructed with local crustal
574 legs and analytical approximations of mantle paths based on the average mantle velocity gradient
575 along an event-station transect [*Zhao* 1993; *Zhao and Xie* 1993]. Therefore, one should not
576 anticipate drastically improved travel time predictions on the basis of 3-D ray tracing through the
577 hybrid velocity model.

578 The degradation of travel time predictions on the basis of the hybrid velocity model
579 (relative to AK135) is a direct indication of the lack of self-consistency of the combined models
580 when using a singular travel time calculation approach (3-D ray tracing in this case). The issue
581 of self-consistency of patchwork regional/teleseismic models may be partially addressed through
582 empirical baseline travel time adjustments [e.g. *Yang et al.* 2004] or more sophisticated empirical
583 travel time or velocity model corrections. However, to achieve the highest level of self-
584 consistency, a singular and seamless tomographic model of the crust and mantle must be created
585 through simultaneous inversion of regional and teleseismic data with the same forward theory for
586 predicting all of the seismic travel time data.

587

588 **5.4. Tomographic Inversion Procedures and Data Predictions**

589 Sensitivities to each of the model nodes defined in the starting solution
590 (RSTT+GyPSuM) were determined based on the calculated 3-D ray paths and model space
591 sensitivity definitions described in previous sections. Also described in a previous section, the
592 starting model is a hybrid combination of multiple P-wave velocity models represented by 55
593 nodesets (layers) and ~1.6 million model nodes. For the inverse problem, we chose to combine
594 certain layers to limit the number of free parameters and account for limited resolvability in
595 particular depth zones. Layers were combined by simply summing sensitivities across multiple
596 layers, thus collapsing the matrix of sensitivity kernels. Specifically, sensitivities to all nodes
597 representing the crust (as defined in the full hybrid model) were summed along the geocentric
598 vertices to define a single set of sensitivity kernels associated with the crust. Therefore,
599 tomographic inversion yields slowness perturbations for the entire crustal stack at each lateral
600 position instead of within each individual crustal layer. The upper mantle sensitivities were
601 condensed in a similar manner creating 9 total inversion layers in the crust and upper mantle with
602 an average effective depth spacing of ~80 km. The lower mantle sensitivity kernels were only
603 slightly condensed providing an average depth spacing of just over 100 km. In total, the number
604 of nodes sensitivities were reduced from ~1.6 million (55 layers) in the forward model to
605 ~600,000 (31 layers) free parameters to be determined in the tomographic inversion process.

606 In order to set up the inversion using the PMTI approach, sensitivity kernels were
607 developed for each tessellation level up to the defining levels in the starting model (Level 7, ~1°
608 spacing, in the crust and upper mantle; Level 6, ~2° spacing, in the lower mantle). The travel
609 time residuals were defined as the *Bayesloc* posteriori travel times minus the predicted travel

610 times based on 3-D ray paths through the hybrid starting model, RSTT+GyPSuM. One of the
611 major assets afforded by the *Bayesloc* procedure is knowledge of the statistics of the full data set
612 and meaningful error estimates for each data point. Thus, the data were weighted according to
613 these error estimates. See *Myers et al*. [2009] and the companion paper in this issue *Myers et al.*
614 [2010b] for more details.

615 Global-scale velocity model updates were determined by carrying out the PMTI
616 procedure where successive inversions were performed using the LSQR algorithm [*Paige and*
617 *Saunders* 1984]. We initiated the progression by solving for model updates at nodes defined by
618 tessellation Level 4 vertices (~8° lateral node spacing) followed by Levels 5,6 and 7 (4°, 2° and
619 1° node spacing, respectively). We chose not to begin the progressive inversion below Level 4
620 to limit structural leakage across drastically different tectonic environments. In addition, we
621 chose not to adjust the depth resolution during the progression. A global damping operator was
622 employed as regularization and the damping weight was chosen based on the trade-off of model
623 norm and data misfit (L-curve analysis).

624 Owing to the substantial non-linearity of ray paths and velocity structure for regional
625 phases, P_n ray paths and sensitivity kernels were re-computed after one complete PMTI cycle
626 and the inversion procedure was performed again. After the 2nd inversion cycle, P_n ray paths
627 were computed once again to test for convergence. It was concluded that most minimum-time
628 ray paths did not change appreciably; and paths that noticeably changed, did not generate
629 substantially different travel time predictions relative to the previous stage. It is our conclusion
630 that the sensitivity definitions, which include multi-pathing and broadened kernels, mitigate the
631 non-linear path-velocity interdependence issues to a large degree. However, we are cautious
632 about generalizing this observation to every scenario and region.

633 Ray paths for upper mantle triplicated phases (~15-22°) are also expected to be strongly
634 dependent upon lateral velocity variations. Before re-computing these ray paths with an updated
635 velocity model, we chose to first consider prior information regarding the topographic variations
636 of the upper mantle transition zone discontinuities. Numerous studies have independently
637 concluded that significant topographic variations of the transition zone discontinuities exist [e.g.
638 *Shearer and Masters* 1992; *Flanagan and Shearer* 1998; *Gurrola and Minster* 1998; *Chevrot et*
639 *al.* 1999; *Lawrence and Shearer* 2008; *Deuss* 2009]. Namely, the '410' km and '660' km
640 discontinuities actually vary in depth by ±30 km or more over relatively short length scales
641 [*Lawrence and Shearer* 2008]. These discontinuity topography fluctuations may lead to
642 incorrect 3-D ray path geometries, incorrect model sensitivity estimates, and therefore inaccurate
643 velocity structure after tomographic inversion is performed. With this issue in mind, we adjusted
644 the depths of the '410' and '660' according to the transition zone discontinuity topographies
645 determined in the global high-resolution *SS* precursor study of *Lawrence and Shearer* [2008].
646 Subsequently, we re-computed all *P* and P_n ray paths (all distance ranges) and performed a final
647 tomographic inversion using the PMTI approach.
648 The final P-wave model, *LLNL-G3Dv1*, predicts the *Bayesloc* posteriori data to within
649 0.50 seconds standard deviation (Figure 10). This equates to ~75% variance reduction relative to
650 *Bayesloc* posteriori travel times predicted with AK135 (1.01 second standard deviation). The
651 initial bulletin data (without *Bayesloc* statistical operations) are predicted to within 3.45 seconds
652 standard deviation on the basis of the 1-D AK135 Earth model. The combination of *Bayesloc*
653 processing and the *LLNL-G3Dv1* velocity model yields data fits on the order of 98% variance
654 reduction relative to the initial data and AK135 (see Figure 10). Thus, the travel times for the
655 ~800,000 *P* and ~42,000 P_n arrivals are predicted to extremely high degrees given the statistical

corrections provided by *Bayesloc* and the 3-D velocity heterogeneities in the new global-scale tomographic model. The misfit to data at upper mantle triplication distances (~15-22°) is relatively high compared to other distance ranges. This result is likely a product of the difficulties in measuring these arrivals and correctly identifying the arrivals that correspond to the theoretical minimum time ray path. Regardless of the issues with triplicated arrivals, the level of data fit is dramatically improved as a result of *Bayesloc* processing and tomographic inversion.

5.5. Model Observations and Interpretations

Large-scale features in the new global P-wave velocity model, *LLNL-G3Dv1*, are illustrated in Figures 12-14. The large-scale heterogeneities, generally observed in past global tomographic investigations, are also seen in our current model. Particularly, in the shallow upper mantle, cratonic roots are found to be fast and spreading centers (such as mid-ocean ridges and rifts) are seismically slow. We also detect broad high-velocity features within the transition zone, along the western Pacific convergent margins, that are likely subducted slabs deflected horizontally along the upper-lower mantle boundary. In the mid-mantle, fast linear anomalies beneath North America and Asia are widely recognized to be associated to the ancient subducted Farallon and Tethyan slabs [e.g. *Grand et al.* 1997; *van der Hilst et al.* 1997]. In the deep mantle, P-wave heterogeneities are dominated by large-scale low-velocity zones associated with the African/Pacific superplume structures and high-velocity zones that might represent subducted slabs that have penetrated into the lower mantle (Figures 13-14).

Most of the major features imaged in the current model are also present in the starting model (GyPSuM) [*Simmons et al.* 2010] as well as our previous global studies [*Simmons et al.*

679 2006, 2007 and 2009]. A significant additional feature emerging in the new model (not clearly
680 seen in GyPSuM) is the apparent subducted slab in the lower mantle beneath the Sea of Japan
681 extending westward beneath the Korean Peninsula and eastern China (Figure 14). The horizontal
682 fast-velocity structures along the base of the upper mantle in this region suggest hindered
683 downward flow of material into the lower mantle. However, the fast anomalies well below the
684 upper mantle suggest that slabs associated with subduction along the northwestern Pacific Ocean
685 occasionally penetrate deep into the mantle as evidenced by numerous tomographic models
686 including global P-wave studies [e.g. *van der Hilst et al.* 1997]. Some of the other major
687 geologic/dynamic features observed in the *LLNL-G3Dv1* model are pointed out in Figure 14.
688 See *Simmons et al.* [2010, in press] for a more comprehensive discussion of the properties of
689 some of the major mantle heterogeneities seen in Figures 12-14. The remainder of the discussion
690 will be focused on the Middle East upper mantle.

691 Although the *LLNL-G3Dv1* P-wave velocity model is global in scope, detailed regional-
692 scale heterogeneities are imaged within the upper mantle beneath the greater Middle East region.
693 Figure 15 highlights the imaged details in the shallowest mantle (just below the Moho) beneath
694 the Middle East and the evolution of the velocity structure through the PMTI process. The Level
695 4 model update (inversion at nodes with ~8° spacing) increases the velocity in the surrounding
696 shield regions relative to the RSTT velocity model [*Myers et al.* 2010a]. Most notably, the
697 Archean/Proterozoic cratonic zones beneath the Baltic shield and East European Platform
698 become exceptionally fast. The shallow mantle beneath India and the Tibetan Plateau become
699 similarly fast. In addition, the velocities beneath the eastern portion of the ancient Arabian
700 shield are significantly increased to values comparable to the P_n tomography study in *Al-Lazki et*
701 *al.* [2004]. Through the PMTI progression shown in Figure 15, low-velocity zones along the

Arabia-Eurasia and India-Eurasia collision zones become increasingly distinct. A number of the focused low-velocity structures in the shallowest mantle can be quickly associated with zones of recent volcanism in the greater Middle East region. In addition, the high-velocity structure along eastern Arabia, interpreted as Precambrian cratonic material, becomes increasingly higher velocity and more sharply defined with each step in the PMTI process.

At a depth of 150 km, the final model differs dramatically from the starting solution in the shallow upper mantle beneath the Middle East region (Figure 16). A number of high-velocity anomalies emerge along the convergent Arabia-Eurasia and India-Eurasia plate boundaries. A broad high-velocity anomaly is evident beneath much of the eastern part of the Arabian continent, likely indicating the existence of ancient continental lithosphere that has not been severely altered by rifting processes occurring along the Red Sea. The thick lithosphere beneath Arabia is connected to high-velocity material that extends several hundred kilometers beneath Iran at a depth of about 150 km (see cross sections along A-A' and B-B' in Figures 16-17). A high-velocity structure is also observed beneath the Makran region of southern Iran and Pakistan; however, the structure does not extend deep into the interior of the Eurasia plate (see the cross section C-C' in Figures 16-17). The lateral extent and connectivity of the high-velocity structures are illustrated more completely with a 3-D view of the seismic heterogeneity (Figure 18).

The collision of the Arabia and Eurasia plates began 16-30 Ma and approximately 300-500 km of convergence has occurred based on plate reconstructions [*Dewey et al.* 1989; *Robertson* 2000; *Allen et al.* 2004]. In the crust, Arabia-Eurasia plate convergence is accommodated by shortening along the continent-continent collision zone as well as distributed deformation throughout Iran and surrounding regions [e.g. *Jackson et al.* 1995; *Allen et al.* 2004;

725 *Paul et al.* 2006; *Reilinger et al.* 2006]. In particular, the continent-continent collision produced
726 the Turkish-Iranian plateau and crustal shortening features such as the Caucasus Mountains
727 (spanning between the Black and Caspian Seas) and the Zagros Mountains that extend from
728 northwestern Iran to the Strait of Hormuz. At depths well below the crust (>100 km), our
729 tomographic model suggests that the Arabia-Eurasia collision results in extensive underthrusting
730 of Arabian lithosphere beneath Iran (see Figure 17). Thus accommodation of the deep
731 lithosphere may be achieved by underthrusting in contrast to shortening processes that
732 accommodate the collision in the shallow lithosphere. Note that the extent of underthrusting
733 beneath Eurasia (based on the cross sections in Figure 17) is on the same order of the proposed
734 maximum plate convergence of 500 km since the initial collision [*Dewey et al.* 1989; *Allen et al.*
735 2004].

736 The continent-continent collision along the western Arabia-Eurasia boundary transitions
737 to an oceanic-continental subduction zone along the southern plate boundary beneath the Makran
738 region of Iran and Pakistan [*Byrne et al*. 1992; *Regard et al.* 2004]. The transition from collision
739 to subduction is manifested at the surface by the termination of the Zagros Mountains near the
740 Strait of Hormuz and the existence of a trench along the Makran subduction zone. More
741 robustly, the transition is marked by seismicity patterns [*Byrne et al* 1992; *Engdahl et al.* 2006]
742 and complex crustal deformation patterns deduced by GPS studies [e.g. *Vernant et al.* 2004;
743 *Reilinger et al.* 2006]. The transition from collision/underthrusting to subduction is also
744 suggested by the modeled upper mantle structures which have two distinct structural orientations
745 (Figures 16, 18). In particular, the fast anomaly beneath Arabia extends to the northeast,
746 generally in line with the plate convergence direction (along the B-B' transect in Figure 16).

747 However, the fast anomaly ~150 km beneath southern Iran and Pakistan has a more east-west
748 orientation, similar to the orientation of the Makran subduction zone trench (Figure 18).
749
750 **6. Conclusions**
751 In this paper we construct a global-scale P-wave tomography model with built-in detailed
752 crustal components including explicit representation of undulating and discontinuous boundaries
753 modified from previous works [*Bassin et al.* 2000; *Pasyanos et al.* 2004; *Steck et al.* 2004]. In
754 addition, the topography of the transition zone discontinuities is explicitly characterized based on
755 the work of *Lawrence and Shearer* [2008]. Moreover, layers are defined in space to conform to
756 the WGS84 ellipsoid and the expected hydrostatic shape of the mantle and core [*Nakiboglu*
757 1982; *Alessandrini* 1989]. This more realistic representation of the crust and mantle allows for
758 accurate prediction of regional and teleseismic travel times via 3-D ray tracing without
759 substantial travel time corrections. The model architecture, based on spherical tessellations, is
760 designed for rapid communication with the model via a hierarchical version of the triangle
761 searching method [*Lawson* 1984]. We further take advantage of the hierarchical nature of the
762 tessellation-based design by development of a tomographic imaging procedure we call
763 *Progressive Multi-level Tessellation Inversion* (PMTI). Similar to wavelet and multi-grid
764 approaches [e.g. *Chiao and Kuo* 2001; *Zhou* 1996], the PMTI method captures long-wavelength
765 structures where data are sparse while details emerge only where the data necessitate. PMTI is a
766 relatively simple, but effective method for imaging seismic structure at multiple length-scales
767 without the subjectivity of dynamic mesh refinement and/or optimization of complex
768 regularization operators.

We show that the global version of the *Bayesloc* multi-event locator [*Myers et al.* 2007, 2009] produces extremely consistent travel time data that are ideal for seismic tomography [see the *Myers et al.* companion paper in this issue]. A tremendous amount of travel time signal that might be interpreted as 3-D structure is shown to be primarily due to errors in event location, phase identification, and travel time measurements. All such errors are statistically modeled by the *Bayesloc* algorithm, providing an extremely valuable method for data culling and weighting for a tomographic inversion.

Our initial monitoring model, named *LLNL-G3Dv1*, is a global-scale tomographic model of P-wave velocity that predicts >800,000 *P* and >42,000 P_n travel times (mostly from Middle East events) to within 0.50 seconds standard deviation. The model is built with the tools and processes described in this paper including: *Bayesloc* data processing, 3-D ray tracing with multi-pathing, and PMTI imaging. The current model consists of large-scale mantle structures such as spreading centers, cratons, superplumes and lower mantle slabs (generally observed in all modern global tomography models). In addition, the image depicts remarkably detailed structures in the upper mantle below the Middle East, owing to the dense data coverage in the region and data consistency yielded by the *Bayesloc* processing. As a result, our model provides a new and important perspective of the upper mantle structures associated with convergence of the Arabia and India plates with Eurasia. In particular, we image the underthrusted continental Arabian lithosphere beneath Iran along the western Arabia-Eurasia plate boundary. In addition, the transition from continent-continent collision to subduction beneath the Makran region along the southern Arabia-Eurasia boundary is evidenced by the imaged structures in the *LLNL-G3Dv1* model. The next phase in this modeling effort will be to perform the same procedures developed and demonstrated in the current study with a massive set of teleseismic *P* travel time data that are

792 more globally distributed than the data considered herein. In conjunction, P_n travel time data
793 from multiple regions will be considered simultaneously for the purpose of self-consistent travel
794 time prediction at both regional and teleseismic distances.
795
796 **Acknowledgments**
797 This work performed under the auspices of the U.S. Department of Energy by Lawrence
798 Livermore National Laboratory under Contract DE-AC52-07NA27344.

799 **References**

800 Alessandrini, B. (1989), The hydrostatic equilibrium figure of the Earth: and iterative approach,
801 *Phys. Earth Planet. Int*., *54*, 180-192.
802 Al-Lazki, A. I., E. Sandvol, D. Seber, M. Barazangi, N. Turkelli and R. Mohamad (2004), P_n
803 tomographic imaging of mantle lid velocity and anisotropy at the junction of the Arabian,
804 Eurasian and African plates, *Geophys. J. Int*., *158*, 1024-1040.
805 Allen, M., J. Jackson and R. Walker (2004), Late Cenozoic reorganization of the Arabia-Eurasia
806 collision and the comparison of short-term and long-term deformation rates, *Tectonics*,
807 *23*, doi:10.1029/2003TC001530.
808 Antolik, M., G. Ekström and A. M. Dziewonski (2001), Global event location with full and
809 sparse data sets using three-dimensional model of mantle P-wave velocity, *Pure Appl.*
810 *Geophys*., *158*, 291-317.
811 Antolik, M., Y. J. Gu, G. Ekström and A. M. Dziewonski (2003), J362D28: a new joint model of
812 compressional and shear velocity in the Earth's mantle, *Geophys. J. Int*., *153*, 443-466.

Ballard, S., J. R. Hipp and C. J. Young (2009), Efficient and accurate calculation of ray theory seismic travel time through variable resolution 3D Earth models, *Seis. Res. Lett*., *80*(6), 990-1000.

Baumgardner, J. R. and P. O. Frederickson (1985), Icosahedral discretization of the two-sphere, *SIAM J. Numer. Anal*., *22*(6), 1107-1115.

Bassin, C., G. Laske and G. Masters (2000), The current limits of resolution for surface wave tomography in North America, *EOS Trans*. AGU, *81*, F897.

Bijwaard, H., W. Spakman and E. R. Engdahl (1998), Closing the gap between regional and global travel time tomography, *J. Geophys. Res*., *103(B12)*, 30,055-30,078.

Bodin, T., M. Sambridge and K. Gallagher (2009), A self-parameterizing partition model approach to tomographic inverse problems, *Inverse Problems*, *25*, doi: 10.1088/0266-5611/25/5/055009.

Boschi, L. and A. M. Dziewonski (1999), High- and low-resolution images of the Earth's mantle: implications of different approaches to tomographic modeling, *J. Geophys. Res*., *104*(B11), 25567-25594.

Boschi, L. (2006), Global multiresolution models of surface wave propagation: comparing equivalently regularized Born and ray theoretical solutions, *Geophys. J. Int*., *167*, 238-252.

Byrne, D. E., L. R. Sykes and D. M. Davis (1992), Great thrust earthquakes and aseismic slip along the plate boundary of the Makran subduction zone, *J. Geophys. Res*., *97*(B1), 449-478.

Chevrot, S., L. Vinnik and J. P. Montagner (1999), Global-scale analysis of the mantle Pds phases, *J. Geophys. Res*., *104*(B9), 20203-20219.

836 Chiao, L. -Y. and B. -Y. Kuo (2001), Multiscale seismic tomography, *Geophys. J. Int.*, *145*, 517-
837 527.
838 Chiao, L. -Y. and W. -T. Liang (2003), Multiresolution parameterization for geophysical inverse
839 problems, *Geophysics*, *68*(1), 199-209.
840 Constable, C. G., R. L. Parker and P. B. Stark (1993), Geomagnetic field models incorporating
841 frozen-flux constraints, *Geophys. J. Int.,, 113*, 419-433.
842 Dahlen, F. A., S. -H. Hung and G. Nolet (2000), Fréchet kernels for finite-frequency traveltimes.
843 I. Theory, *Geophys. J. Int.*, *141*, 157-174.
844 DeMets, C., R. G. Gordon, D. F. Argus and S. Stein (1994), Effects of recent revisions to the
845 geomagnetic reversal time scale on estimates of current plate motions, *Geophys. Res.*
846 *Lett.*, *21*, 2191-2194.
847 Deuss, A. (2009), Global observations of mantle discontinuities using SS and PP precursors,
848 *Surv. Geophys.*, *30*, 301-326.
849 Dewey, J. F., M. L. helman, E. Turco, D. H. W. Hutton and S. D. Knott (1989), Kinematics of
850 the western Mediterranean, in Alpine Tectonics, edited by M. P. Coward, D. Dietrich and
851 R. G. Park, *Geol. Soc. Spec. Publ.*, *45*, 265-283.
852 Dziewonski, A. M., B. H. Hager and R. J. O'Connell (1977), Large scale heterogeneities in the
853 lower mantle, *J. Geophys. Res.*, *82*, 239-255.
854 Dziewonski, A. M. and D. L. Anderson (1981), Preliminary reference Earth model, *Phys. Earth*
855 *Planet. Inter.*, *25*, 297-356.
856 Engdahl, E. R., R. van der Hilst and R. Buland (1998), Global teleseismic earthquake relocation
857 with improved travel times and procedures for depth determination, *Bull. Seis. Soc.*
858 *Amer.*, *88*(3), 722-743.

859 Engdahl, E. R., J. A. Jackson, S. C. Myers, E. A. Bergman and K. Priestly (2006), Relocation
860 and assessment of seismicity in the Iran region, *Geophys. J. Int*., *167*, 761-778.
861 Flanagan, M. P. and P. M. Shearer (1998), Global mapping of topography on transition zone
862 velocity discontinuities by stacking of SS precursors, *J. Geophys. Res*., *103*(B2), 2673-
863 2692.
864 Grand, S. P., R. D. Van der Hilst and S. Widiyantoro (1997), Global seismic tomography: a
865 snapshot of convection in the Earth, *GSA Today*, *7*, 1-7.
866 Grand, S. P. (2002), Mantle shear-wave tomography and the fate of subducted slabs, *Phil. Trans.*
867 *R. Soc. Lond. A*, *360*(1800), 2475-2491.
868 Gu, Y. J., A. M. Dziewonski, W. Su & G. Ekstrom (2001), Models of the mantle shear velocity
869 and discontinuities in the pattern of lateral heterogeneities, *J. Geophys. Res.*, *106*, 11169-
870 11199.
871 Gung, Y., Y. -T. Hsu, L. -Y. Chiao and M. Obayashi (2009), Multiscale waveform tomography
872 with two-step parametermization, *J. Geophys. Res*., *114*, doi: 10.1029/2008JB006275.
873 Gurrola, H. and J. B. Minster (1998), Thickness estimates of the upper-mantle transition zone
874 from bootstrapped velocity spectrum stacks of receiver functions, *Geophys. J. Int*., *133*,
875 31-43.
876 Husen, S. and E. Kissling (2001), Local earthquake tomography between rays and waves: fat ray
877 tomography, *Phys. Earth Planet. Int*., *125*, 171-191.
878 Inoue, H., Y. Fukao, K. Tanabe and Y. Ogata (1990), Whole mantle P-wave travel time
879 tomography, *Phys. Earth Planet. Inter*., *59*, 294-298.
880 Ishii, M. and J. Tromp (1999), Normal-mode and free-air gravity constraints on lateral variations
881 in velocity and density of Earth's mantle, *Science*, *285*(5431), 1231-1236.

882 Ishii, M. and A. M. Dziewonski (2002), The innermost inner core of the Earth: Evidence for a
883 change in anisotropic behavior at the radius of about 300 km, *PNAS*, *99*(22), 14026-
884 14030.
885 Jackson, J., J. Haines and W. Holt (1995), The accommodation of Arabia-Eurasia plate
886 convergence in Iran, *J. Geophys. Res*., *100*(B8), 15,205-15,219.
887 Kárason, H. & R. D. van der Hilst (2000), Constraints on mantle convection from seismic
888 tomography, in: M. R. Richards, M. R. Gordon, R. D. van der Hilst (Eds.), The History
889 and Dynamics of Global Plate Motion, AGU, Washington, DC, pp. 277-288.
890 Kennett, B. L. N., E. R. Engdahl and R. Buland (1995), Constraints on seismic velocities in the
891 Earth from travel times, *Geophys. J. Int*., *122*, 108-124.
892 Kennett, B. L. N. and A. Gorbatov (2004), Seismic heterogeneity in the mantle—strong shear
893 wave signature of slabs from joint tomography, *Phys. Earth Planet. Inter.*, *146*, 87-100.
894 Lawrence, J. G. and P. M. Shearer (2008), Imaging mantle transition zone thickness with *SdS-SS*
895 finite-frequency sensitivity kernels, *Geophys. J. Int*., *174*, 143-158.
896 Lawson, C. L. (1984), C^1 surface interpolation for scattered data on a sphere, *J. Mathematics*,
897 *14*(1), 177-202.
898 Li, C., R. D. van der Hilst, E. R. Engdahl and S. Burdick (2008), A new global model for P wave
899 speed variations in Earth's mantle, *Geochem. Geophys. Geosys*., *9*(5), doi:
900 10.1029/2007GC001806.
901 Masters, G., G. Laske, H. Bolton & A. M. Dziewonski (2000), The relative behavior of shear
902 velocity, bulk sound speed, and compressional velocity in the mantle: implications for
903 chemical and thermal structure, *in Earth's Deep Interior: Mineral Physics and*

Tomography from the Atomic to the Global Scale, edited by S. -I. Karato et al., pp. 63-87, AGU, Washington, DC.

Mégnin, C. & B. Romanowicz (2000), The three-dimensional shear velocity structure of the mantle from the inversion of body, surface and higher-mode waveforms, *Geophys. J. Int.*, *143*, 709-728.

Mooney, W. D., G. Laske & G. Masters (1998), CRUST 5.1: a global crustal model at 5 x 5 degrees, *J. Geophys. Res. Solid Earth*, *103*(B1), 727-747.

Moritz, H. (1980), Geodetic reference system 1980, *Bull. Géodésique Paris*, *54*(3), 5 pp.

Myers, S. C., G. Johannesson and W. Hanley (2007), A Bayesian hierarchical method for multiple-event seismic location, *Geophys. J. Int*., *171*, 1049-1063.

Myers, S. C., G. Johannesson and W. Hanley (2009), Incorporation of probabilistic seismic phase labels into a Bayesian multiple-event seismic locator, *Geophys. J. Int*., *177*, 193-204.

Myers, S. C., M. L. Begnaud, S. Ballard, M. E. Pasyanos, W. S. Phillips, A. L. Ramirez, M. S. Antolik, K. D. Hutchenson, J. J. Dwyer, C. A. Rowe and G. S. Wagner (2010a), A crust and upper-mantle model of Eurasia and North Africa for P_n travel-time calculation, *Bull. Seis. Soc. Amer*., *100*(2), 640-656.

Myers, S. C., G. Johannesson and N. A. Simmons (2010b), Global-scale P-wave tomography optimized for prediction of teleseismic and regional travel times for Middle East events: 1. Data set development*, J. Geophys. Res.,* (companion paper).

Nakiboglu, S. M. (1982), Hydrostatic theory of the Earth and its mechanical implications, *Phys. Earth Planet. Int*., *28*, 302-311.

926 Nolet, G. and R. Montelli (2005), Optimal paraterization of tomographic models, *Geophys. J.*
927 *Int.*, *161*, 365-372.
928 Paige, C. C. and M. A. Saunders (1982), LSQR: an algorithm for sparse linear equations and
929 sparse least squares, *ACM Transactions on Mathematical Software*, *8*, 43-71.
930 Pasyanos, M. E., W. R. Walter, M. P. Flanagan, P. Goldstein and J. Bhattacharyya (2004),
931 Building and testing an a priori geophysical model for Western Eurasia and North Africa,
932 *Pure Appl. Geophys*., *161*, 235-281.
933 Pasyanos, M. E., G. A. Franz and A. L. Ramirez (2006), Reconciling a geophysical model to
934 data using a Markov chain Monte Carlo algorithm: An application to the Yellow Sea-
935 Korean Peninsula region, *J. Geophys. Res.*, *111*, doi: 10.1029/2005JB003851.
936 Paul, A., A. Kaviani, D. Hatzfeld, J. Vergne and M. Mokhtari (2006), Seismological evidence for
937 crustal-scale thrusting in the Zagros mountain belt (Iran), *Geophys. J. Int*., *166*, 227-237.
938 Regard, V. *et al.* (2004), Accommodation of Arabia-Eurasia convergence in the Zagros-Makran
939 transfer zone, SE Iran: A transition between collision and subduction through a young
940 deforming system, *Tectonics*, *23*(TC4007), doi:10.1029/2003TC001599.
941 Reilinger, R. *et al.* (2006), GPS constraints on continental deformation in the Africa-Arabia-
942 Eurasia continental collision zone and implications for the dynamics of plate interactions,
943 *J. Geophys. Res*., *111*(B05411), doi:10.1029/2005JB004051.
944 Ritsema, J., H. J. Van Heijst and J. H. Woodhouse (1999), Complex shear wave velocity
945 structure imaged beneath Africa and Iceland, *Science*, *286*(5446) 1925-1928.
946 Ritzwoller, M. H., N. M. Shapiro, A. L. Levshin, E. A. Bergman and E. R. Engdahl (2003),
947 Ability of a global three-dimensional model to locate regional events, *J. Geophys. Res*.,
948 *108*(B7), doi: 10.1029/2002JB002167.

949 Robertson, A. H. F. (2000), Mesozoic-Tertiary tectonic-sedimentary evolution of a south
950 Tethyan oceanic basin and its margins in southern Turkey, in *Tectonics and Magmatism*
951 *in Turkey and the Surrounding Area*, edited by E. Bozkurt, J. A. Winchester and J. D. A.
952 Piper, *Geol. Soc. Spec. Publ.*, *173*, 97-138.
953 Robertson, G. S. and J. H. Woodhouse (1996), Ratio of relative S to P velocity heterogeneity in
954 the lower mantle, *J. Geophys. Res*., *101*, 20041-20052.
955 Romanowicz, B. (1991), Seismic tomography of the Earth's mantle, *Annu. Rev. Earth Planet.*
956 *Sci*., *19*, 77-99.
957 Romanowicz, B. (2003), Global mantle tomography: Progress status in the past 10 years, *Annu.*
958 *Rev. Earth Planet. Sci*., *31*, 303-328.
959 Ruppert, S., D., Dodge, A. Elliott, M. Ganzberger, T. Hauk and E. Matzel (2005), Enhancing
960 seismic calibration research through software automation and scientific information
961 management, in *Proceedings of the 27th Seismic Research Review: Ground-Based*
962 *Nuclear Explosion Monitoring Technologies,* LA-UR-05-6407, Vol. 2.
963 Sambridge, M. and R. Faletič (2003), Adaptive whole Earth tomography, *Geochem. Geophys.*
964 *Geosys*., *4*(3), doi:10.1029/2001GC000213.
965 Sengupta, M. K. and M. N. Toksöz (1976), Three-dimensional model of seismic velocity
966 variation in the Earth's mantle, *Geophys. Res. Lett*., *3*, 84-86.
967 Shearer, P. M. and G. Masters (1992), Global mapping of topography on the 660-km
968 discontinuity, *Nature*, *355*, 791-796.
969 Simmons, N. A., A. M. Forte and S. P. Grand (2006), Constraining mantle flow with seismic and
970 geodynamic data: a joint approach, *Earth Planet. Sci. Lett*. *246*, 109–124.

971 Simmons, N. A., A. M. Forte and S. P. Grand (2007), Thermochemical structure and dynamics
972 of the African superplume, *Geophys. Res. Lett., 34*(2), L02301, doi:
973 10.1029/2006GL028009.
974 Simmons, N. A., A. M. Forte and S. P. Grand (2009), Joint seismic, geodynamic and mineral
975 physical constraints on three-dimensional mantle heterogeneity: implications for the
976 relative importance of thermal versus compositional heterogeneity, *Geophys. J. Int*.
977 *177*(5), 1284–1304.
978 Simmons, N. A., A. M. Forte, L. Boschi and S. P. Grand (2010), GyPSuM: A joint tomographic
979 model of mantle density and seismic wave speeds, *J. Geophys. Res*., (in press).
980 Spakman, W. and H. Bijwaard (2001), Optimization of cell parameterizations for tomographic
981 inverse problems, *Pure Appl. Geophys*., *158*, 1401-1423.
982 Steck, L. K., C. A. Rowe, M. L. Begnaud, W. S. Phillips, V. L. Gee and A. A. Velasco (2004),
983 Advancing seismic event location through difference constraints and three-dimensional
984 models, *Proceedings of the 26th Seismic Research Review*, Orlando, Florida, September
985 2004.
986 Stockmann, R. C. C. Finlay and A. Jackson (2009), Imaging Earth's crustal magnetic field with
987 satellite data: a regularized spherical triangle tessellation approach, *Geophys. J. Int*., *179*,
988 929-944.
989 Trampert, J., F. Deschamps, J. Resovsky and D. Yuen (2004), Probabilistic tomography maps
990 chemical heterogeneities throughout the lower mantle, *Science*, *306*(5697), 853-856.
991 Um, J. and C. Thurber (1987), A fast algorithm for two-point seismic ray tracing, *Bull. Seis. Soc.*
992 *Amer*., *77*, 972-986.

van der Hilst, R. D., S. Widiyantoro and E. R. Engdahl (1997), Evidence for deep mantle circulation from global tomography, *Nature*, *386*, 578-584.

Vernant, P. *et al.* (2004), Present-day crustal deformation and plate kinematics in the Middle East constrained by GPS measurements in Iran and northern Oman, *Geophys. J. Int*., *157*, 381-398.

Wang, Z. and F. A. Dahlen (1995), Spherical-spline parameterization of three-dimensional Earth models, *Geophys. Res. Lett*., *22*(22), 3099-3102.

Widiyantoro, S., B. L. N. Kennett and R. D. van der Hilst (1998), Extending shear-wave tomography for the lower mantle using *S* and *SKS* arrival-time data, *Earth Planets and Space*, *50(11-12)*, 999-1012.

Yang, X., I. Bondár, J. Bhattacharyya, M. Ritzwoller, N. Shapiro, M. Antolik, G. Ekström, H. Israelsson and K. McLaughlin (2004), Validation of regional and teleseismic travel-time models by relocating ground-truth events, *Bull. Seis. Soc. Amer*., *94*(3), 897-919.

Zhao, D., A. Hasegawa, and S. Horiuchi (1992), Tomographic imaging of P and S wave velocity structure beneath northeastern Japan, *J. Geophys. Res*., *97*, 19909–19928.

Zhao, D. (2001), Seismic structure and origin of hotspots and mantle plumes, *Earth Planet. Sci. Lett. 192*, 251-265.

Zhao, D. and J. Lei (2004), Seismic ray path variations in a 3D global velocity model, *Phys. Earth Planet. Int*., *141*, 153-166.

Zhao, L. -S. (1993), Lateral variations and azimuthal isotropy of P_n velocities beneath Basin and Range province*, J. Geophys. Res*., *98*, 22109-22122.

Zhao, L. -S. and J. Xie (1993), Lateral variations in compressional velocities beneath the Tibetan Plateau from P_n travel time tomography, *Geophys. J. Int*., *115*, 1070-1084.

1016 Zhou, H. -W. (1996), A high-resolution *P* wave model for the top 1200 km of the mantle, *J.*
1017 *Geophys. Res.*, *101*(B12), 27791-27810.
1018 Zhou, H. -W. (2004), Multi-scale tomography for crustal *P* and *S* velocities in southern
1019 California, *Pure Appl. Geophys*., *161*, 283-302.
1020

Figure Captions

Figure 1. Spherical tessellation grids and parent-daughter triangle relationships. The initial object (a regular icosahedron; Level 1) consists of 20 triangular faces and 12 distinct vertices. The triangular faces (parents) are recursively subdivided into smaller triangles (daughters) and the vertices are normalized to the unit sphere. Each recursion represents a level in the tessellation hierarchy and parent-daughter triangle relationships are indexed for efficient communication. Triangular regions are shaded simply for visual orientation of the parent-daughter regions and sub-regions.

Figure 2. Model referencing and node architecture. **(a-b)** A hierarchical triangle searching algorithm is used to establish the vertices that surround a unit vector in the direction of the point-of-interest, $\hat{\mathbf{p}}$. Barycentric coordinates are inherently determined at each step in the hierarchical search providing lateral interpolation weights at all tessellation levels (see text). **(c)** Model nodes are placed at arbitrary radii in the direction of the tessellation vertices allowing for representation of irregular surfaces. To determine radial interpolation weights, radial profiles are determined along $\hat{\mathbf{p}}$ by lateral interpolation of radii for surrounding points (R_1 interpolated from $r_{1,a-c}$ and R_2 interpolated from $r_{2,a-c}$). The distances of R_1 and R_2 from the point-of-interest (POI) provide the simple radial interpolation weights, and any model property can then be determined.

Figure 3. One-dimensional synthetic test case used to demonstrate the PMTI modeling procedure described in the text. **(top)** Six equally spaced nodes were placed along a line to represent the 1st recursion level. Points were then placed at the midpoints between the 1st level points to construct the 2nd recursion level set of nodes. This recursion was repeated once again to

1044 give a total of 21 node points and a total of 3 tessellation levels. **(middle)** Seismic velocities
1045 were assigned to the nodes to imitate the uppermost mantle P-wave velocity structure,
1046 transitioning from a platform/shield environment (with fast, long-wavelength velocity structure)
1047 to a tectonically active environment (with lower overall velocity and shorter wavelength
1048 heterogeneities). **(bottom)** A single realization of the randomly generated set of paths designed
1049 to create an ill-posed tomographic imaging problem. For each realization, 100 1-D ray paths
1050 were generated such that at least 95 paths were entirely beyond 600 km in the X-direction.

1051

1052 **Figure 4.** An example comparison of inversion techniques for the 1-D synthetic model design
1053 shown in Figure 3. Travel times were computed along each of the paths shown in Figure 3 and
1054 30% (RMS) random noise was incorporated to generate a single synthetic data realization. **(left**
1055 **column)** Simple least-squares inversions were performed at each recursion level individually. In
1056 order to capture the regional velocity trend, the nodes defined by the Level 1 tessellation would
1057 suffice (top left). However, a finer parameterization is required to capture the details in the
1058 tectonically active part of our synthetic model space (see Figure 3). **(right column)** The PMTI
1059 procedure solves for the low-resolution model (defined by the Level 1 nodes, top right) and
1060 continues to the next resolution level by reducing the travel time signals on the basis of the
1061 previous lower-resolution model and velocity anomalies accumulate (see text). Within the
1062 synthesized platform/shield environment, simple inversion fails to reproduce the known
1063 structure, particularly if the Level 3 nodes are active in the inversion. However, the PMTI
1064 approach produces a smooth, long-wavelength trend in the poorly sampled platform region while
1065 also reproducing the shorter wavelength features within the tectonically-active environment.
1066 Note that simple damping was used to regulate the systems and damping weights were

1067 independently optimized for each inversion style to produce models with the lowest level of
1068 RMS misfit to the known solution.

1069

1070 **Figure 5.** Comprehensive comparison of simple and PMTI modeling approaches for the 1-D
1071 synthetic test case shown in Figures 3-4. For a chosen damping weight and noise level, we
1072 randomly generated 100 1-D ray paths (similar to the example in Figure 3) 100 times and added
1073 random noise. For each realization of paths and noise, we performed both inversion procedures
1074 and computed the RMS misfit to the known solution. This process was repeated for a discrete
1075 set of damping weights and RMS noise levels of 0, 15 and 30%. The PMTI approach most often
1076 produces solutions closer to the known velocity model regardless of the noise level and chosen
1077 damping weight. The optimal range of damping weights tends to be larger for the PMTI
1078 procedure owing to the intrinsic regularization.

1079

1080 **Figure 6.** Synthetic tomography scenario imitating a combination of regional and teleseismic
1081 phases and complex shallow upper mantle velocity structure parameterized by a triangular
1082 tessellation with 5 hierarchical levels. **(left)** Synthesized velocity structure with a regional trend
1083 (from left to right) and embedded, small-scale velocity heterogeneities. **(center)** Map view of
1084 synthetic ray path coverage consisting of several clusters of sub-horizontal regional phase ray
1085 paths and 3 clusters of near-vertical teleseismic ray paths (highlighted with green circles). **(right)**
1086 3-D view of the synthesized ray path coverage.

1087

Figure 7. Representative tomography solutions for the synthetic tomography scenario shown in Figure 6. Synthetic travel time data were derived from the ray paths shown in Figure 6 and 20% RMS noise was incorporated. For the simple least squares inversion, we incorporated damping and smoothing operators independently and optimized the regularization weights to produce the best possible model (based on RMS model misfit). **(left column)** Synthetic model and 3 possible solutions using different approaches and regularization. With damping alone ('SIMPLE damping'), detailed structures emerge where there are sufficient crossing paths. Isolated velocity structures are generated where there are gaps in ray path coverage. Thus, blobs and streaks are created and the regional velocity trend is not recovered. Simple inversion with a first-order smoothing operator ('SIMPLE smoothing') recovers the long-wavelength regional trend, but fails to recover fine details where information is sufficient. Using the PMTI approach ('PMTI Level 5'), the regional trend is recovered and details emerge where there is sufficient ray path coverage (in the northern portion of the model domain). **(right column)** The accumulation of velocity structure through the PMTI process. The Level 1 inversion (top) recovers the long-wavelength regional velocity trend. Note that the solution changes only slightly through the first 3 progressions (Levels 1-3). These slight changes demonstrate the potential pitfalls of dynamic mesh refinement that would likely cease to insert new model nodes, thereby never recovering the fine (yet resolvable) details.

Figure 8. Seismic events and stations used in this study and processed with the *Bayesloc* algorithm [*Myers et al*. 2010, this issue] **(top)** We consider 5,401 seismic events including all Middle East events with arrival times recorded in the LLNL database and the best-recorded events within 5° bins globally from the EHB catalog

(ftp://ciei.colorado.edu/pub/user/engdahl/EHB). Approximately 4,400 of the seismic events are within the black box drawn on the map. **(bottom)** Approximately 4,500 globally distributed seismic stations were used in this study including ~1,100 stations within the black outlined area.

Figure 9. Data coverage in the greater Middle East region. **(top)** P_n ray path coverage, seismic stations (blue triangles) and seismic events (red circles). **(middle)** P_n hit count map at 150 km depth below the spheroid plotted in log scale. For this study, P_n phases were only considered in the region shown. **(bottom)** Teleseismic *P* phase hit count at 150 km depth below the spheroid in the greater Middle East region. *P* phase coverage is global in extent, but the plot is limited to the region shown to demonstrate the excellent sampling in the Middle East region.

Figure 10. Travel time residuals for the compiled *P* and P_n data set. Residual travel times are plotted as a function of great circle distance in terms of point density on a normalized log scale. **(top left)** Travel time residuals for the initial EHB bulletin and LLNL data set with respect to (w.r.t.) the AK135 1-D velocity model. **(top right)** Travel time residuals w.r.t AK135 after *Bayesloc* processing that includes hypocenter relocation, phase label re-assignments, outlier removal, and statistically based travel time corrections. See *Myers et al.* [2010] in this issue for more detail. **(bottom left)** Residuals based on *Bayesloc* processed data relative to the hybrid regional-teleseismic velocity model described in the text (RSTT+GyPSuM). The hybrid global 3-D velocity model offers no improvement in the prediction of the data set relative to the 1-D AK135 velocity model. **(bottom right)** Travel time residuals w.r.t. to the global 3-D P wave model constructed in this study (*LLNL-G3Dv1*).

Figure 11. Three-dimensional ray tracing procedure adapted from *Zhao et al.* [1992] and seismic sensitivity definitions. **(top)** Several trial ray paths are tested to seek out the global minimum travel time. We perform a limited number of pseudo-bending [*Um and Thurber* 1987] and piercing point adjustment iterations on a set of simple starting paths (black dashed lines). Ray paths that provide travel times within some time tolerance (black solid lines) are further refined through bending and piercing point adjustments until only slight improvement (reduction) in travel times is observed (green dashed and solid lines). The minimum time path can then be selected from the set (green solid line). **(bottom)** Example 3-D ray paths calculated through the global velocity model constructed in this study. All computed ray paths that produce travel times within a given time tolerance of the minimum time path were used in the development of sensitivity kernels. Sensitivity is spread across broad depth zones and/or multiple model units to mitigate the problem of interdependence of paths and velocity structure as well as multi-pathing.

Figure 12. Maps of upper mantle velocity structure from the *LLNL-G3Dv1* global P-wave velocity model constructed in this study. The black box indicates the region with detailed structures shown in Figure 15-16.

Figure 13. Maps of lower mantle velocity structure from the *LLNL-G3Dv1* global P-wave velocity model constructed in this study. A number of the major features are pointed out in Figure 14.

Figure 14. Selected 360° cross sections through the *LLNL-G3Dv1* velocity model. Most of the major features highlighted are also observed in the hybrid starting model based on the joint seismic-geodynamic image called GyPSuM [Simmons et al. 2010, submitted]. However, a number of additional features are observed in the *LLNL-G3Dv1* model including apparent deep slabs originating from the Japan subduction zone and detailed upper mantle structures beneath the Middle East region (see Figures 15-18).

Figure 15. Close-up view of the mantle P-wave velocity at the Moho (shallowest mantle) from the *LLNL-G3Dv1* model. The evolution of the velocity structure within the Progressive Multi-level Tessellation Inversion (PMTI) process is shown. The starting velocity model, RSTT [*Myers et al.* 2010a], is updated by solving for slowness perturbations on a coarse grid (Level 4 tessellation, ~8° node spacing). The model is subsequently updated on progressively finer grids defined by the Level 5 tessellation (~4° spacing), Level 6 tessellation (~2° spacing), and Level 7 tessellation (~1° spacing) to construct the final model. The arrow shows the Arabian plate motion relative to Eurasia from NUVEL-1A [*DeMets et al.* 1994]. Plate boundaries are courtesy of the PLATES Project at the Institute for Geophysics at the University of Texas at Austin.

Figure 16. Close-up view of the P-wave velocity at 150 km depth from the *LLNL-G3Dv1* model. The final model differs dramatically from the starting solution in the shallow upper mantle beneath the Middle East region. Most notably, several high-velocity structures emerge beneath the region and correlate well with the location of deep earthquakes used in this study. These high-velocity features are likely depicting underthrusted/subducted Arabian and Indian lithosphere beneath the Eurasia plate. Cross sections along the A-A', B-B' and C-C' transects are shown in Figure 17.

Figure 17. Cross sections along the A-A', B-B' and C-C' transects shown in Figure 16. Velocity perturbations are relative to the global mean velocity anomalies in *LLNL-G3Dv1* at each depth. High-velocity structures extending from Arabia to beneath Eurasia represent underthrusted continental lithosphere along the western plate boundary and subducted oceanic lithosphere beneath the Makran region along the southern plate boundary.

Figure 18. Three-dimensional perspective of the velocity structures beneath the Middle East region. **(top)** Map view of contoured fast and slow blobs in the upper mantle. The contours are +1.8%, +1.3%, and -1.0% velocity perturbations relative to the global mean velocity anomalies in *LLNL-G3Dv1*. **(bottom)** Same as the top panel, but with the low-velocity zones removed to reveal the full lateral extent of the high-velocity structures and the connectivity of the ancient Arabian shield material to fast structures beneath Iran. The Strait of Hormuz marks the transition from continent-continent collision (creating the Zagros Mountains) and oceanic-continental subduction beneath the Makran region of Iran and Pakistan.

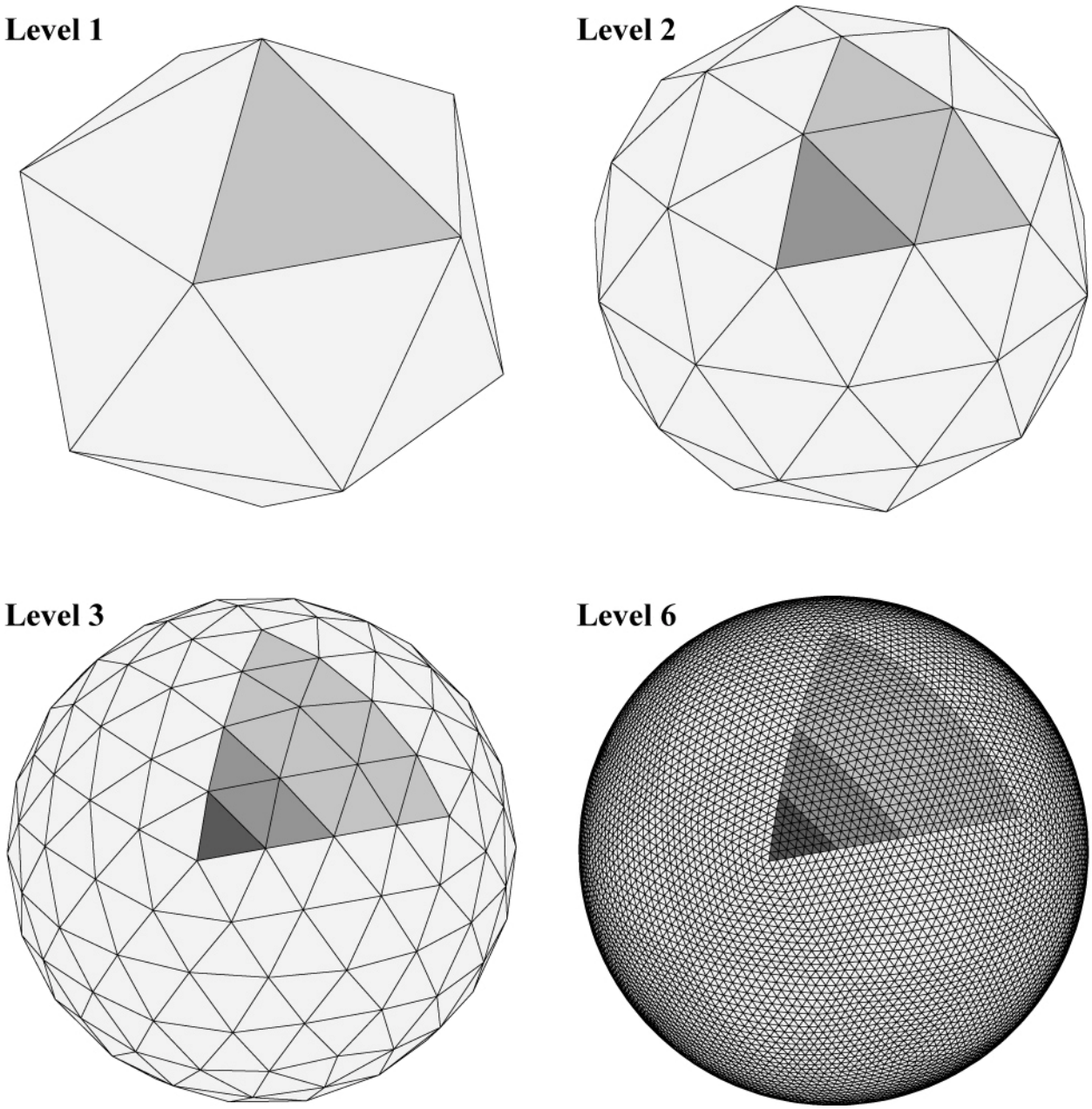

Figure 1

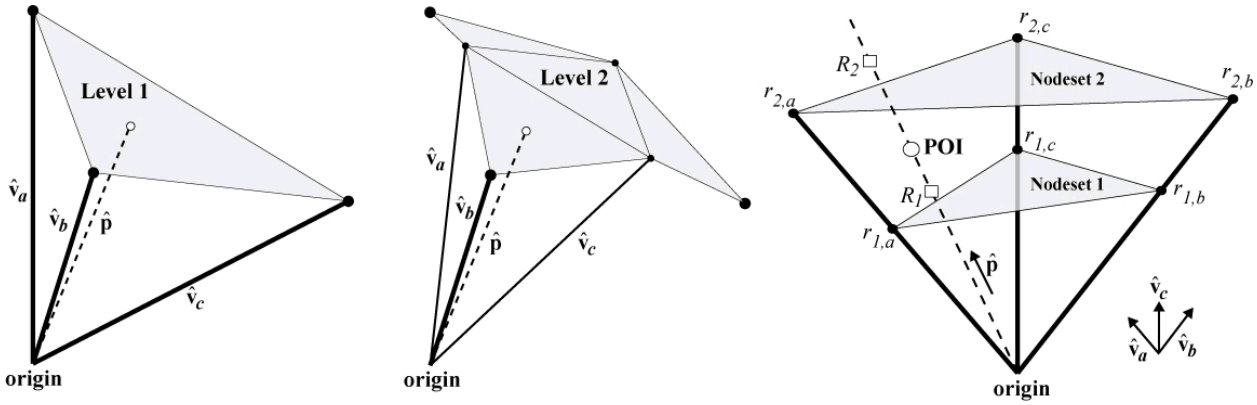
Level 1
$\hat{\mathbf{v}}_a$
$\hat{\mathbf{v}}_b$
$\hat{\mathbf{p}}$
$\hat{\mathbf{v}}_c$
origin
Level 2
$\hat{\mathbf{v}}_a$
$\hat{\mathbf{v}}_b$
$\hat{\mathbf{p}}$
$\hat{\mathbf{v}}_c$
origin
$r_{2,c}$
R_2
Nodeset 2
$r_{2,a}$
$r_{2,b}$
POI
$r_{1,c}$
Nodeset 1
R_1
$r_{1,b}$
$r_{1,a}$
$\hat{\mathbf{p}}$
$\hat{\mathbf{v}}_c$
$\hat{\mathbf{v}}_a$
$\hat{\mathbf{v}}_b$
origin

Figure 2

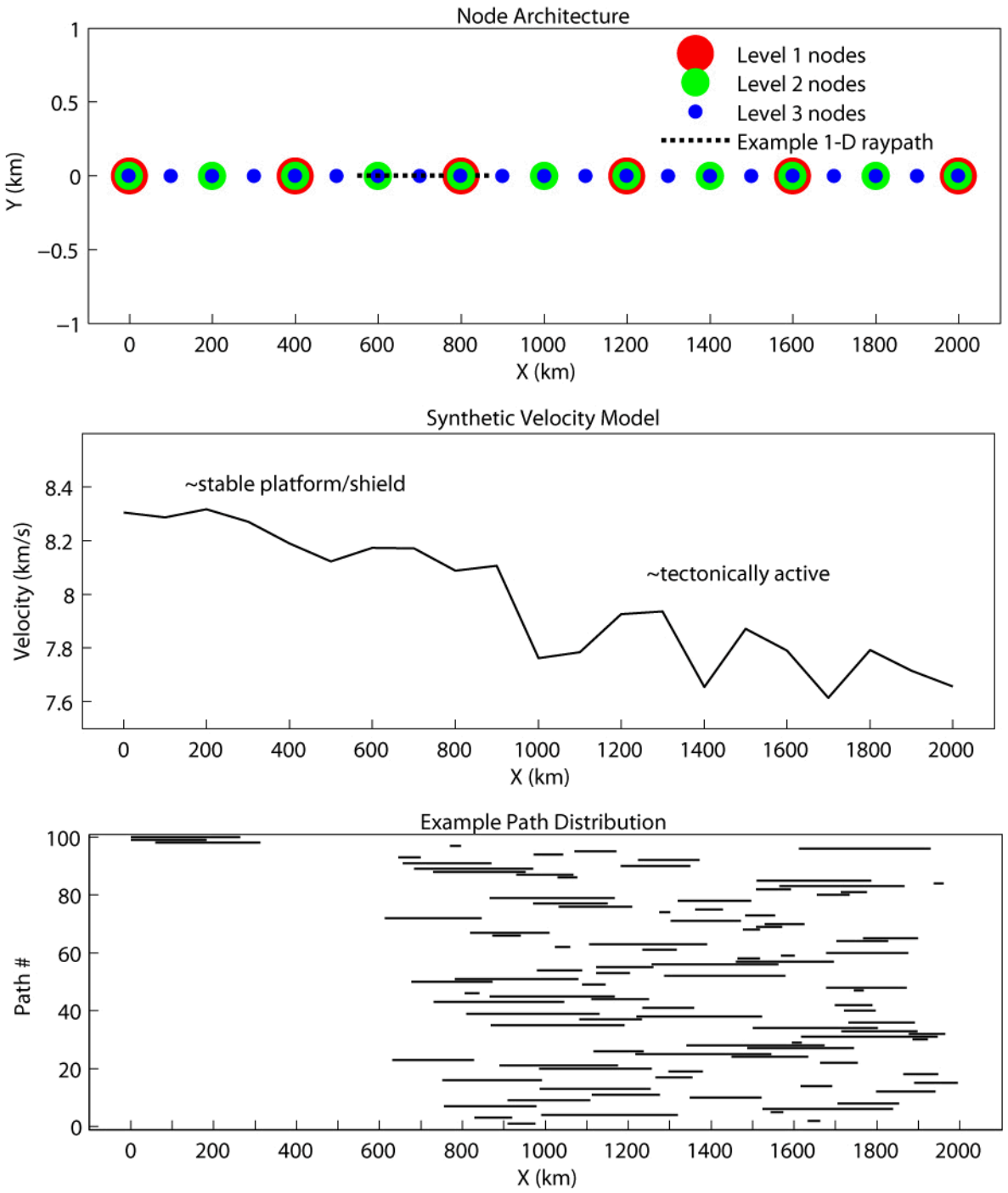
Node Architecture
Level 1 nodes
Level 2 nodes
Level 3 nodes
Example 1-D raypath
Y (km)
X (km)
Synthetic Velocity Model
~stable platform/shield
~tectonically active
Velocity (km/s)
X (km)
Example Path Distribution
Path #
X (km)

Figure 3

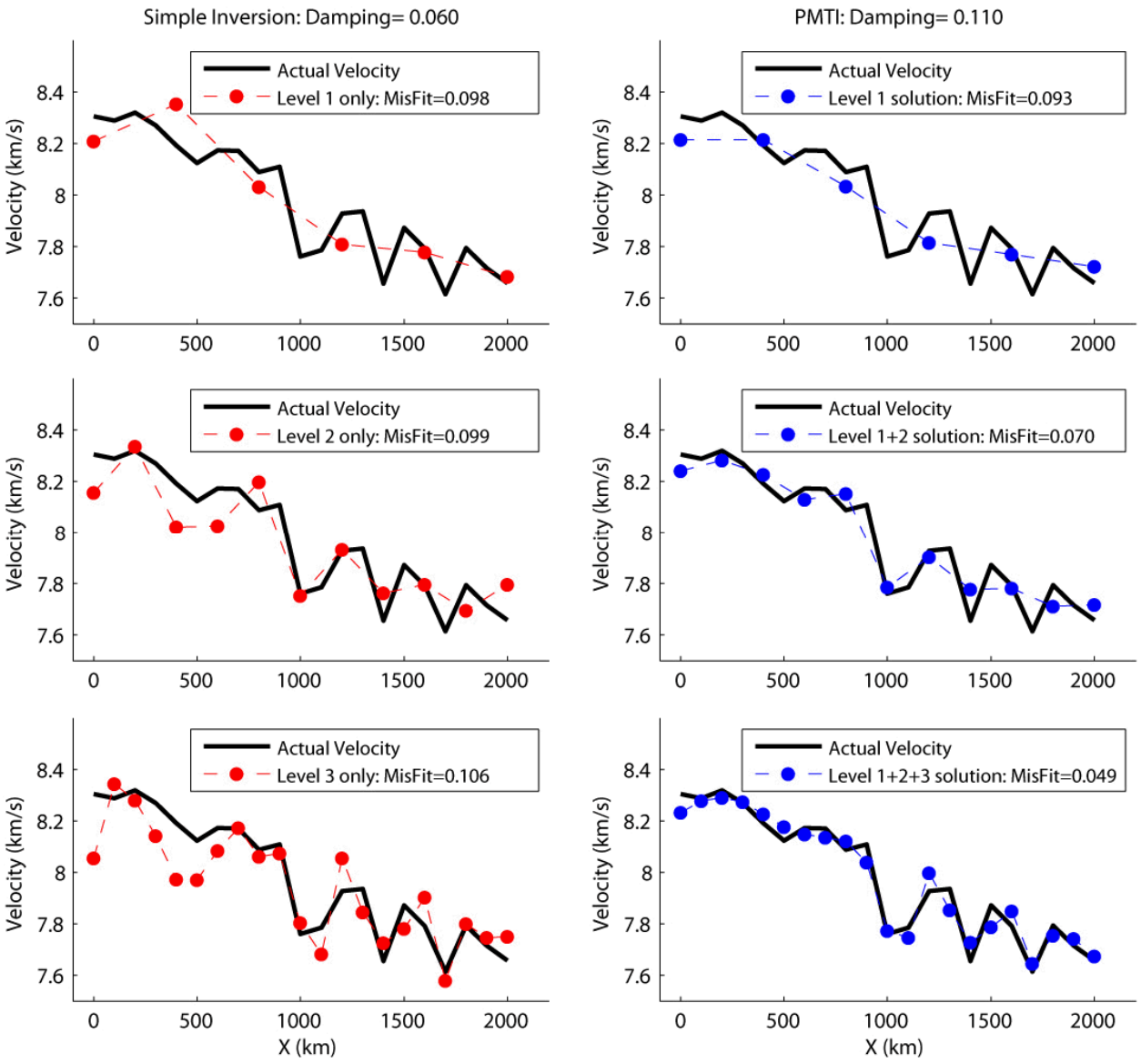
Simple Inversion: Damping= 0.060
PMTI: Damping= 0.110
Actual Velocity
Level 1 only: MisFit=0.098
Level 1 solution: MisFit=0.093
Level 2 only: MisFit=0.099
Level 1+2 solution: MisFit=0.070
Level 3 only: MisFit=0.106
Level 1+2+3 solution: MisFit=0.049
Velocity (km/s)
X (km)
8.4
8.2
8
7.8
7.6
0
500
1000
1500
2000

Figure 4

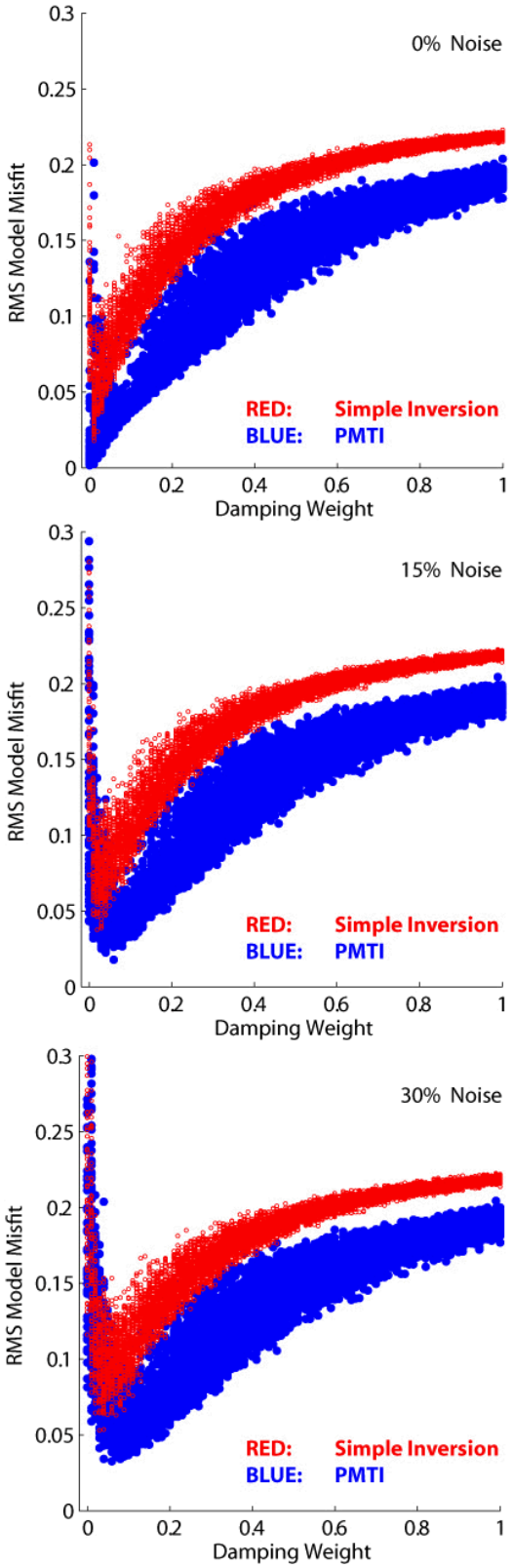
0% Noise
RMS Model Misfit
Damping Weight
RED: Simple Inversion
BLUE: PMTI
15% Noise
RMS Model Misfit
Damping Weight
RED: Simple Inversion
BLUE: PMTI
30% Noise
RMS Model Misfit
Damping Weight
RED: Simple Inversion
BLUE: PMTI

Figure 5

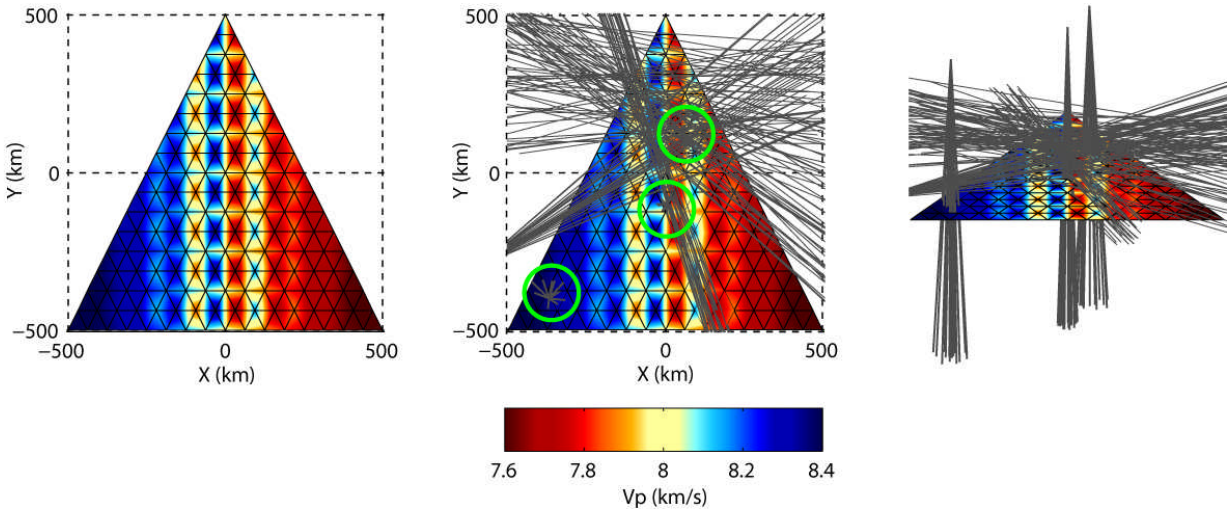
500
0
−500
Y (km)
−500
0
500
X (km)
500
0
−500
Y (km)
−500
0
500
X (km)
7.6
7.8
8
8.2
8.4
Vp (km/s)

Figure 6

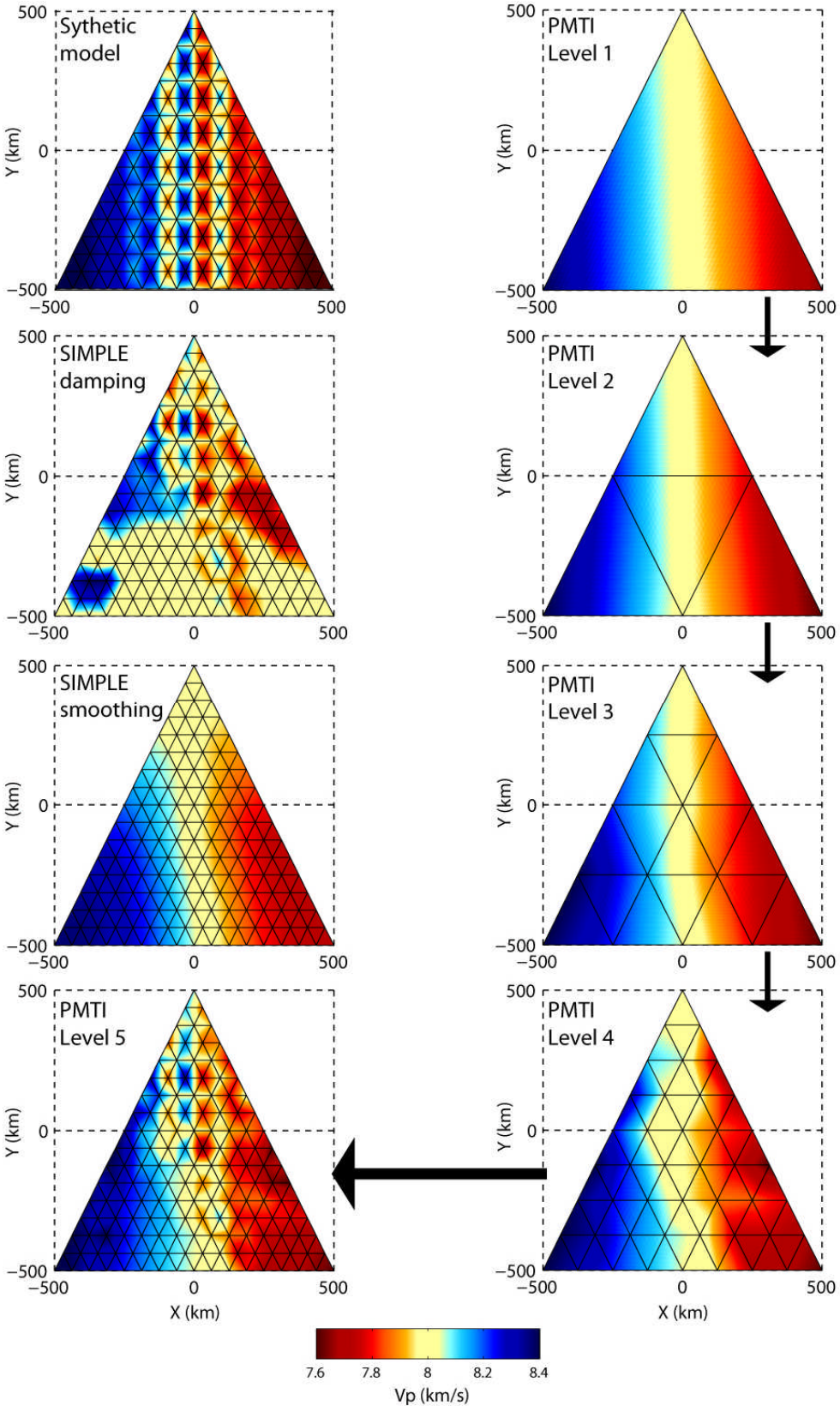
Sythetic model
PMTI Level 1
SIMPLE damping
PMTI Level 2
SIMPLE smoothing
PMTI Level 3
PMTI Level 5
PMTI Level 4
Y (km)
X (km)
500
0
−500
7.6
7.8
8
8.2
8.4
Vp (km/s)

Figure 7

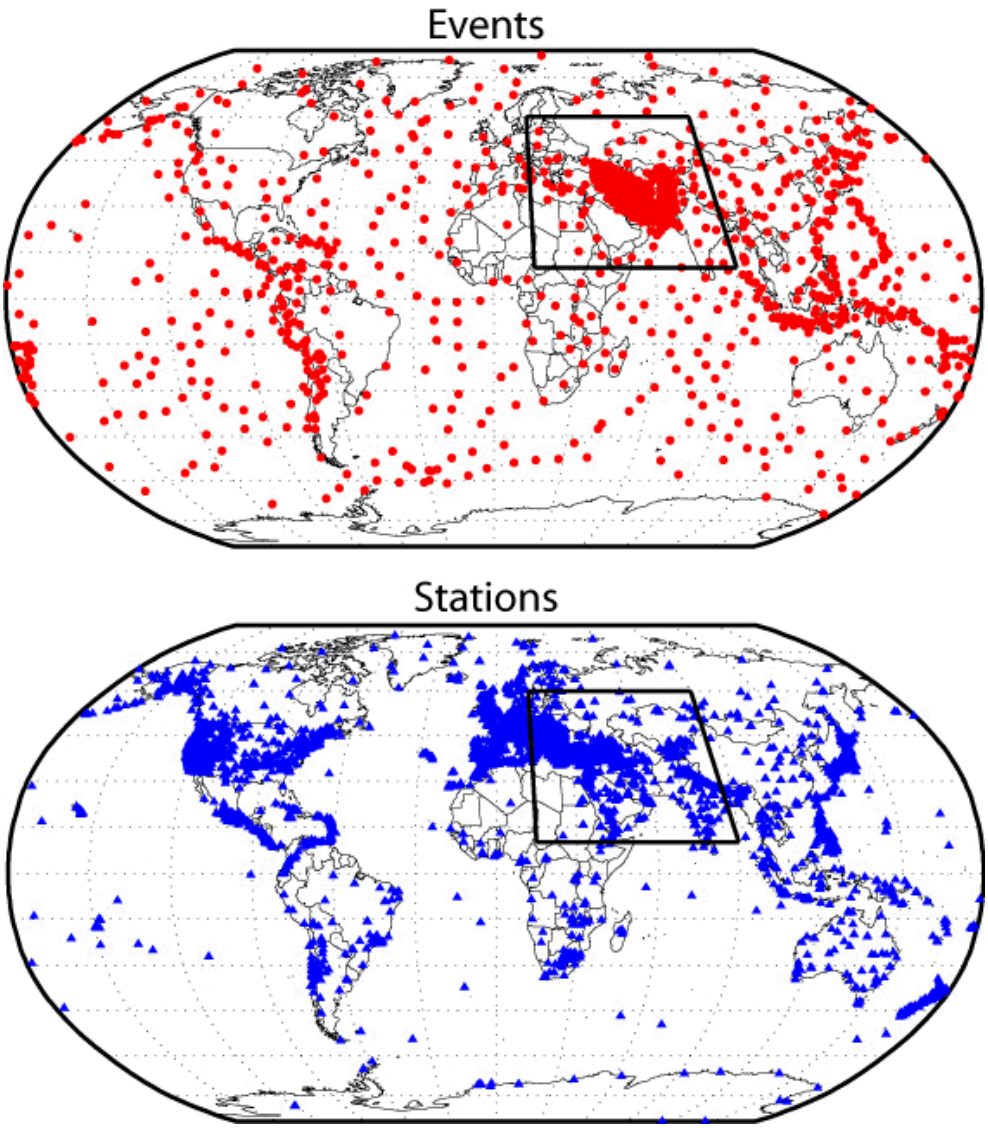

Figure 8

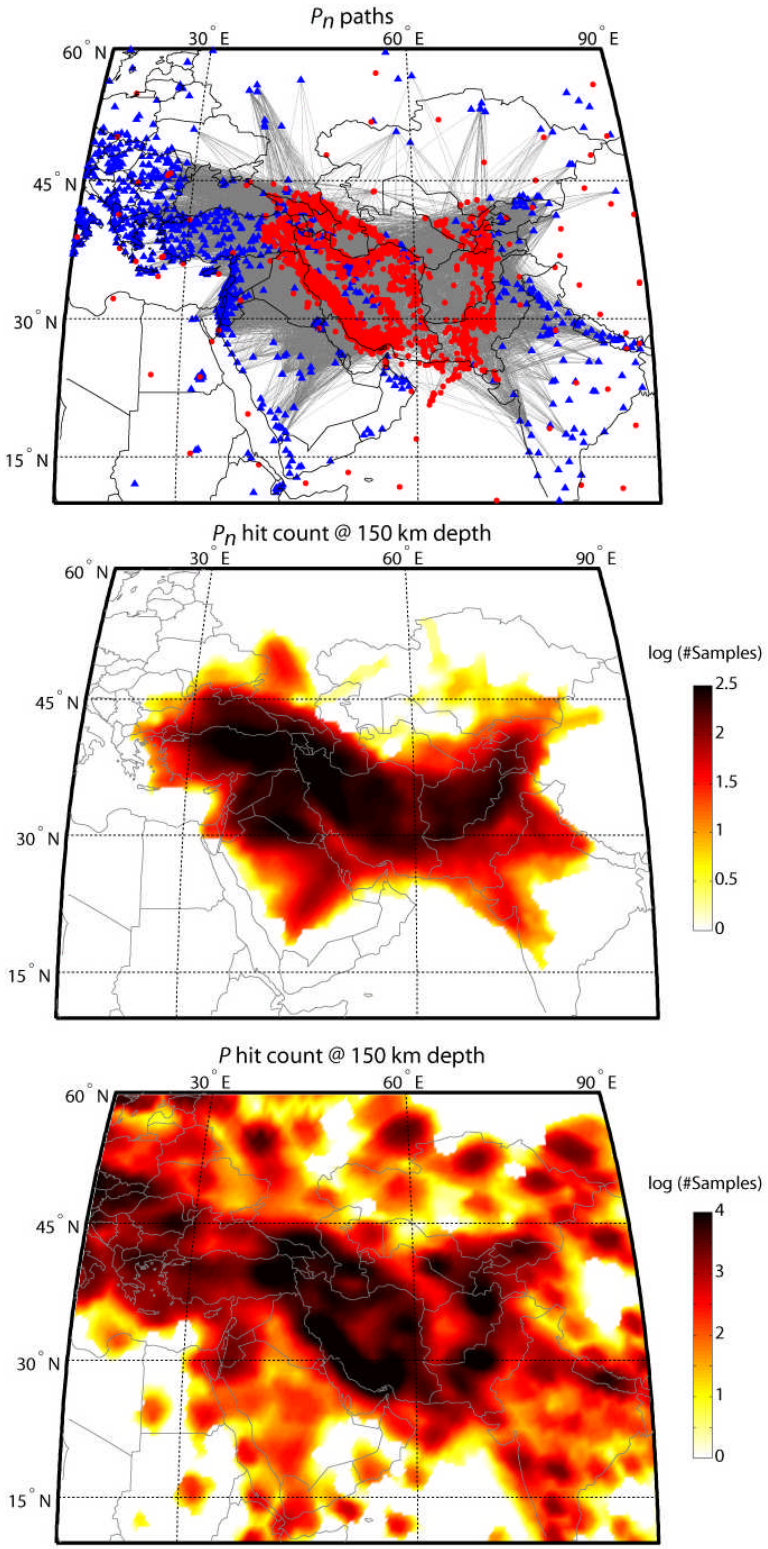
P_n paths
60° N
30° E
60° E
90° E
45° N
30° N
15° N
P_n hit count @ 150 km depth
log (#Samples)
2.5
2
1.5
1
0.5
0
P hit count @ 150 km depth
log (#Samples)
4
3
2
1
0

Figure 9

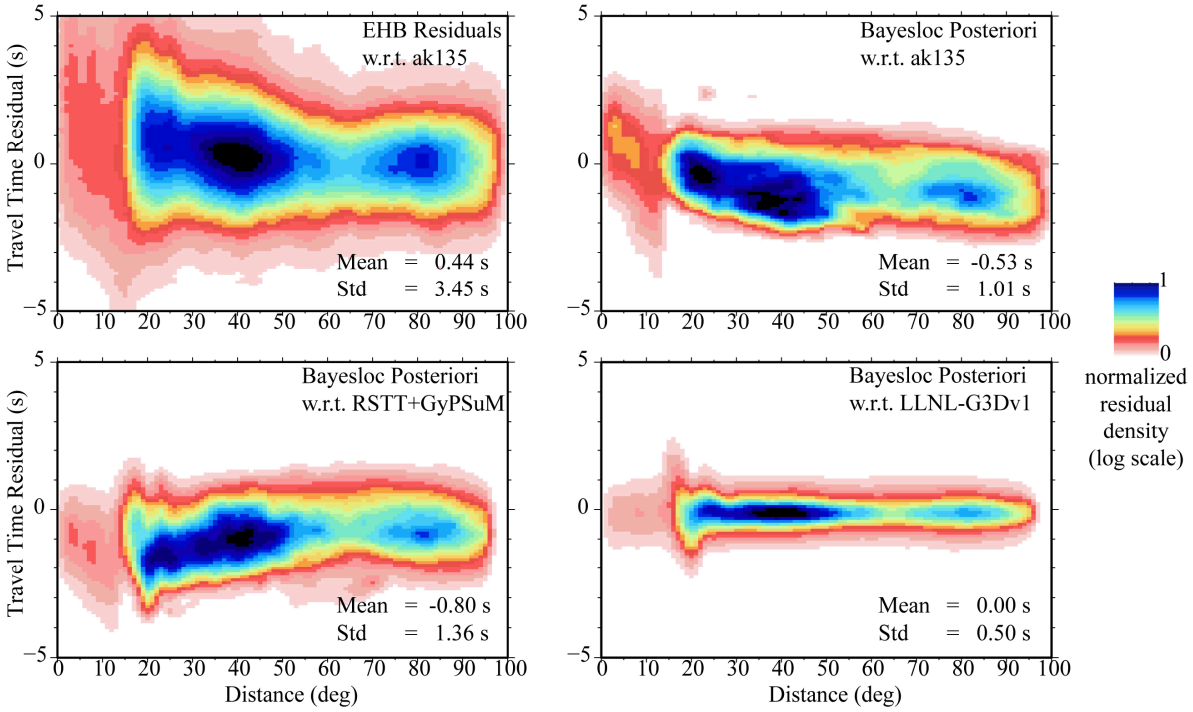
EHB Residuals
w.r.t. ak135
Mean = 0.44 s
Std = 3.45 s
Bayesloc Posteriori
w.r.t. ak135
Mean = -0.53 s
Std = 1.01 s
Bayesloc Posteriori
w.r.t. RSTT+GyPSuM
Mean = -0.80 s
Std = 1.36 s
Bayesloc Posteriori
w.r.t. LLNL-G3Dv1
Mean = 0.00 s
Std = 0.50 s
Travel Time Residual (s)
Distance (deg)
normalized residual density (log scale)

Figure 10

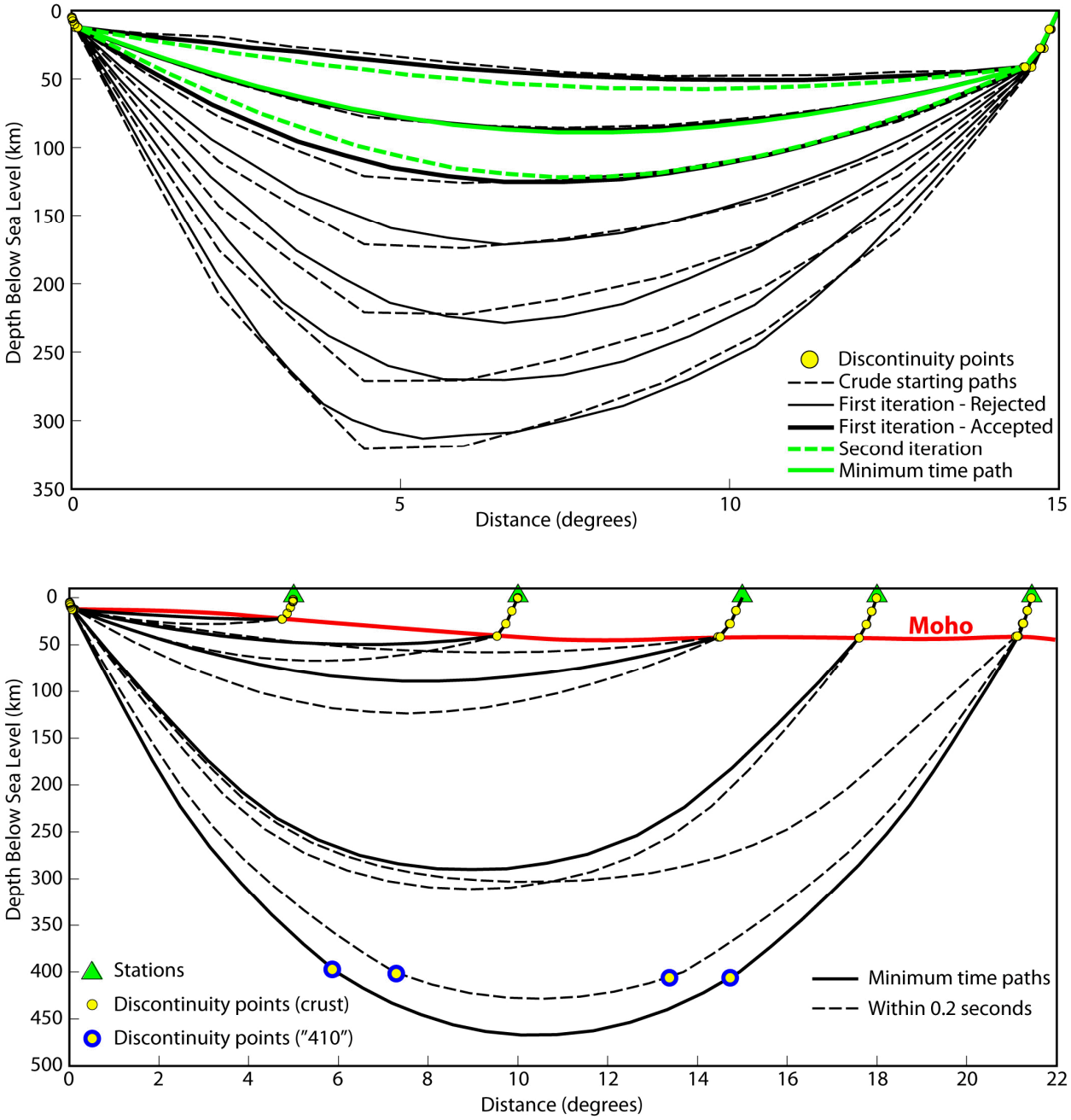
Depth Below Sea Level (km)
Distance (degrees)
Discontinuity points
Crude starting paths
First iteration - Rejected
First iteration - Accepted
Second iteration
Minimum time path
Moho
Stations
Discontinuity points (crust)
Discontinuity points ("410")
Minimum time paths
Within 0.2 seconds

Figure 11

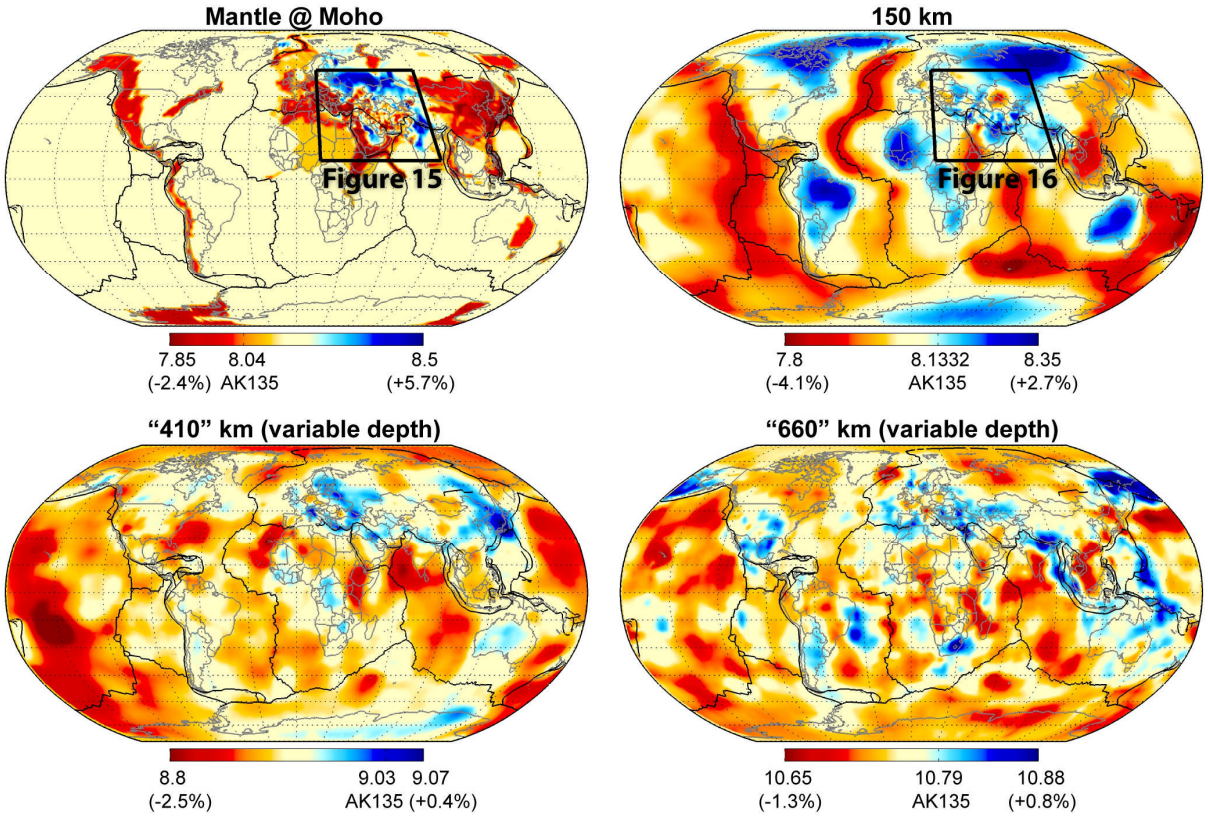
Mantle @ Moho
Figure 15
7.85
(-2.4%)
8.04
AK135
8.5
(+5.7%)
150 km
Figure 16
7.8
(-4.1%)
8.1332
AK135
8.35
(+2.7%)
“410” km (variable depth)
8.8
(-2.5%)
9.03
AK135 (+0.4%)
9.07
“660” km (variable depth)
10.65
(-1.3%)
10.79
AK135
10.88
(+0.8%)

Figure 12

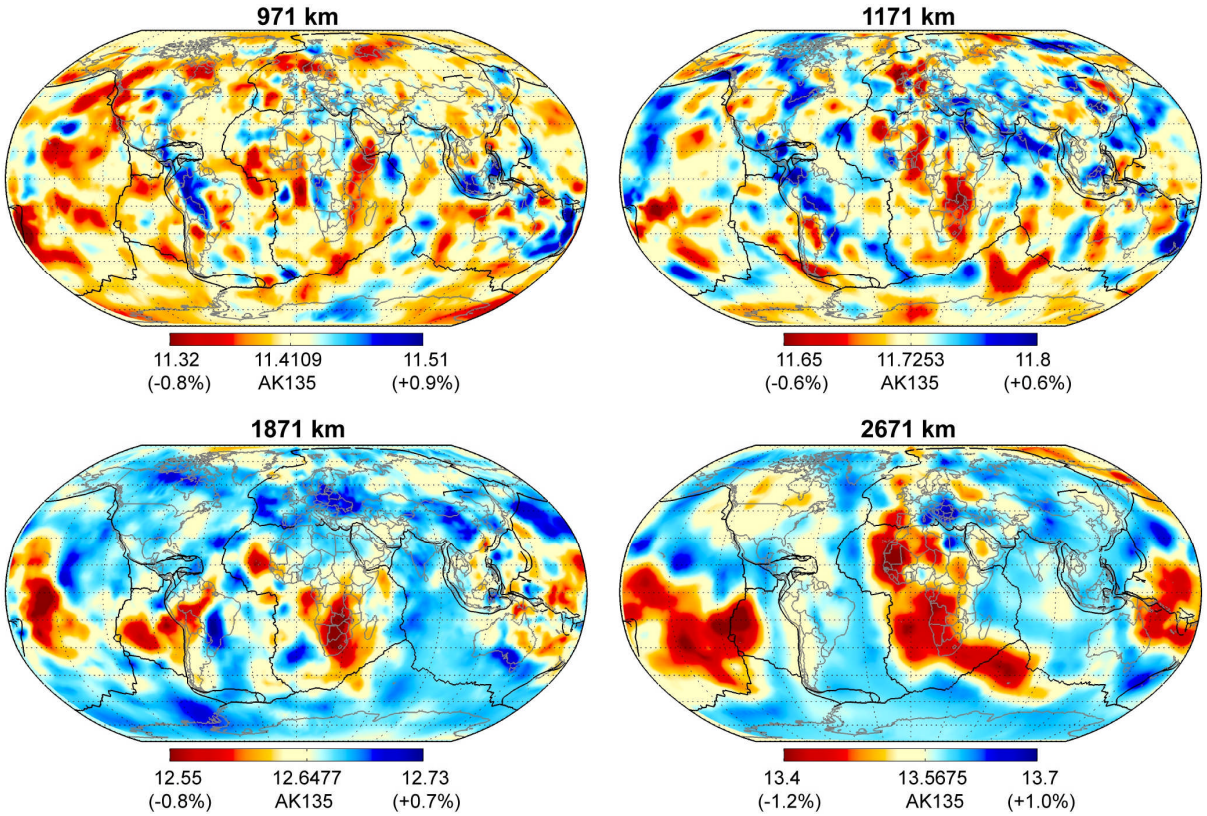
971 km
11.32
(-0.8%)
11.4109
AK135
11.51
(+0.9%)
1171 km
11.65
(-0.6%)
11.7253
AK135
11.8
(+0.6%)
1871 km
12.55
(-0.8%)
12.6477
AK135
12.73
(+0.7%)
2671 km
13.4
(-1.2%)
13.5675
AK135
13.7
(+1.0%)

Figure 13

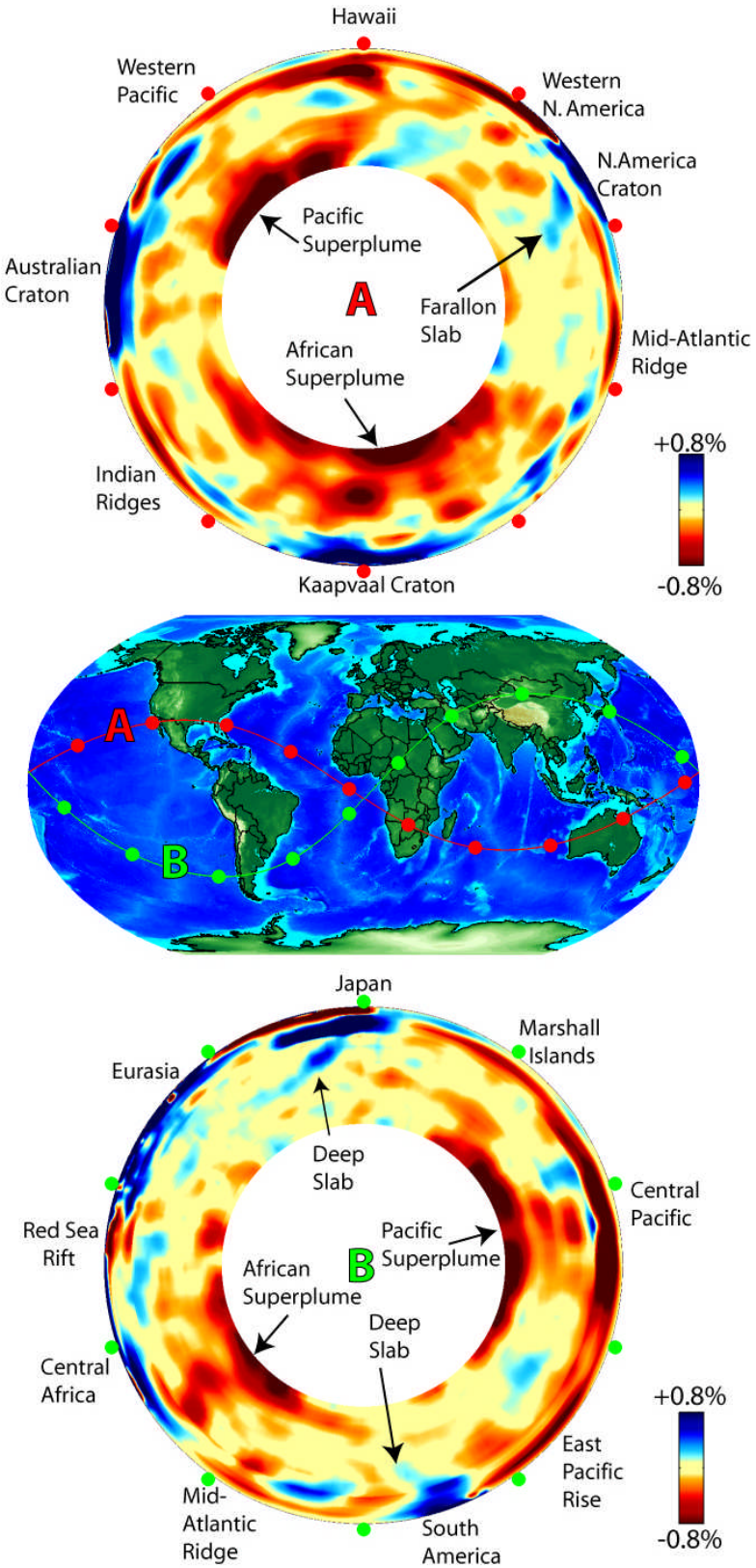
Hawaii
Western Pacific
Western N. America
N.America Craton
Pacific Superplume
A
Farallon Slab
Australian Craton
African Superplume
Mid-Atlantic Ridge
Indian Ridges
Kaapvaal Craton
+0.8%
-0.8%
A
B
Japan
Marshall Islands
Eurasia
Deep Slab
Central Pacific
Red Sea Rift
Pacific Superplume
B
African Superplume
Deep Slab
Central Africa
East Pacific Rise
Mid-Atlantic Ridge
South America
+0.8%
-0.8%

Figure 14

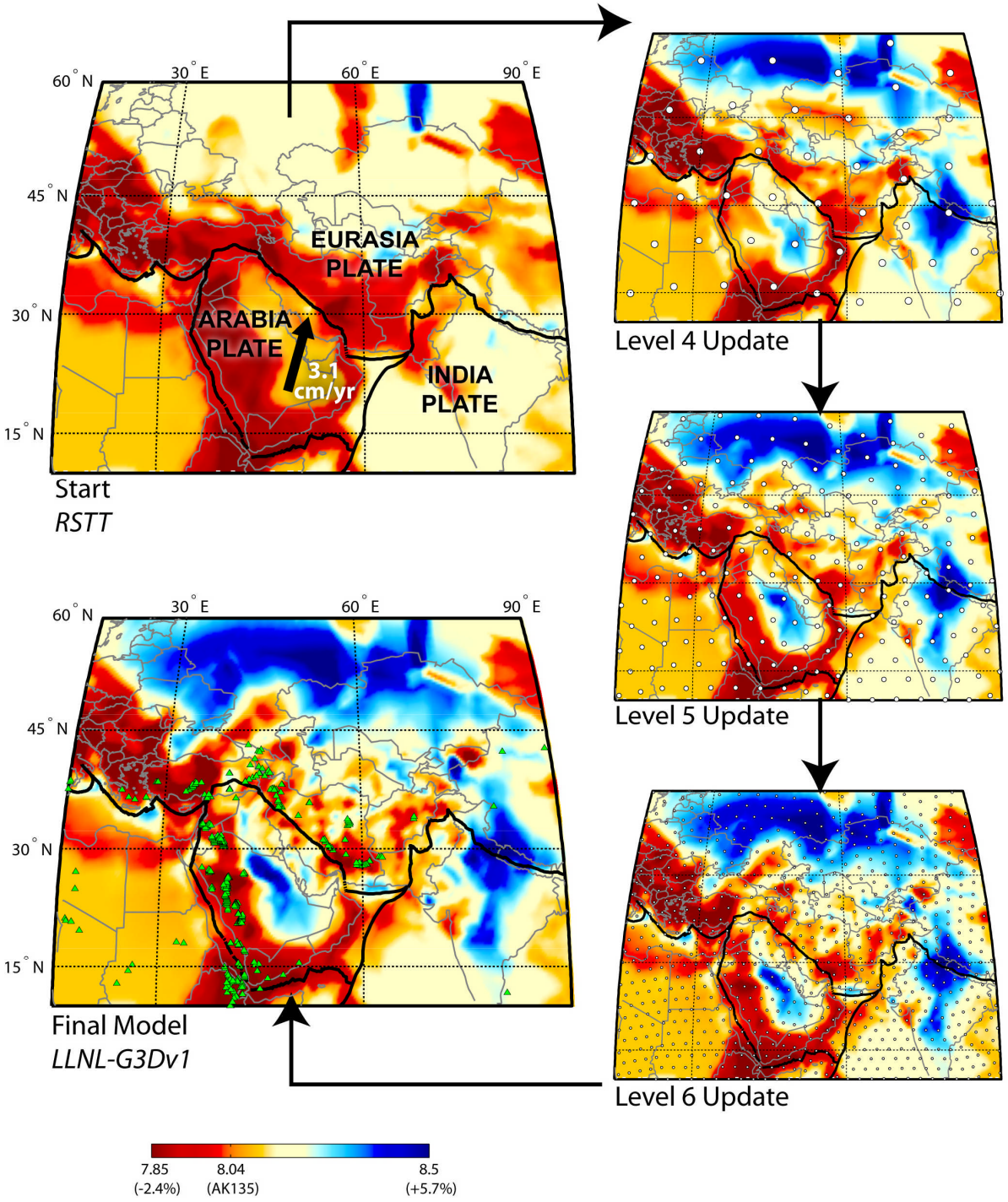
60° N
30° E
60° E
90° E
45° N
30° N
15° N
EURASIA PLATE
ARABIA PLATE
3.1 cm/yr
INDIA PLATE
Start
RSTT
Level 4 Update
Level 5 Update
Level 6 Update
Final Model
LLNL-G3Dv1
7.85
(-2.4%)
8.04
(AK135)
8.5
(+5.7%)

Figure 15

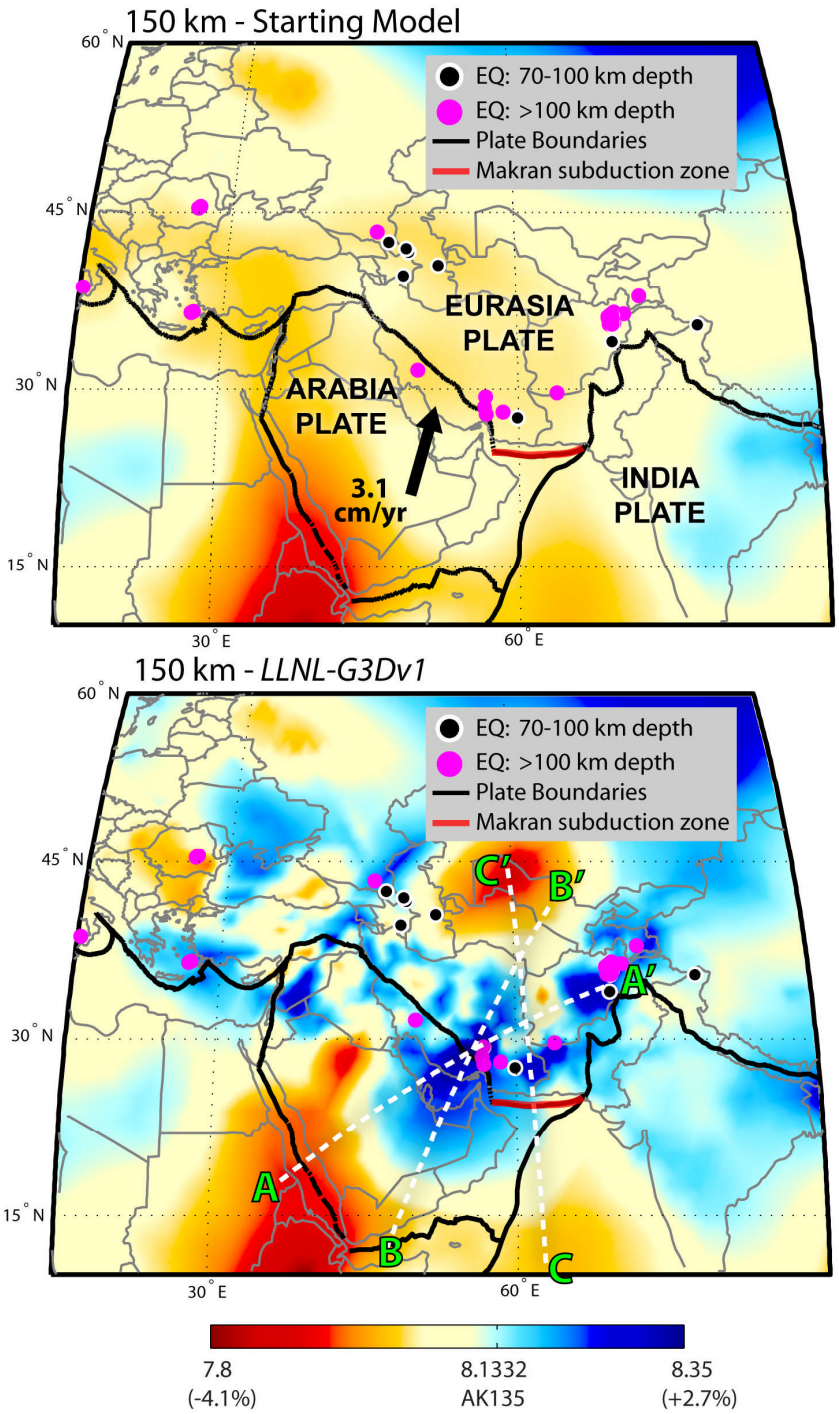
150 km - Starting Model
EQ: 70-100 km depth
EQ: >100 km depth
Plate Boundaries
Makran subduction zone
EURASIA PLATE
ARABIA PLATE
INDIA PLATE
3.1 cm/yr
60° N
45° N
30° N
15° N
30° E
60° E
150 km - LLNL-G3Dv1
EQ: 70-100 km depth
EQ: >100 km depth
Plate Boundaries
Makran subduction zone
A
B
C
A′
B′
C′
7.8
(-4.1%)
8.1332
AK135
8.35
(+2.7%)

Figure 16

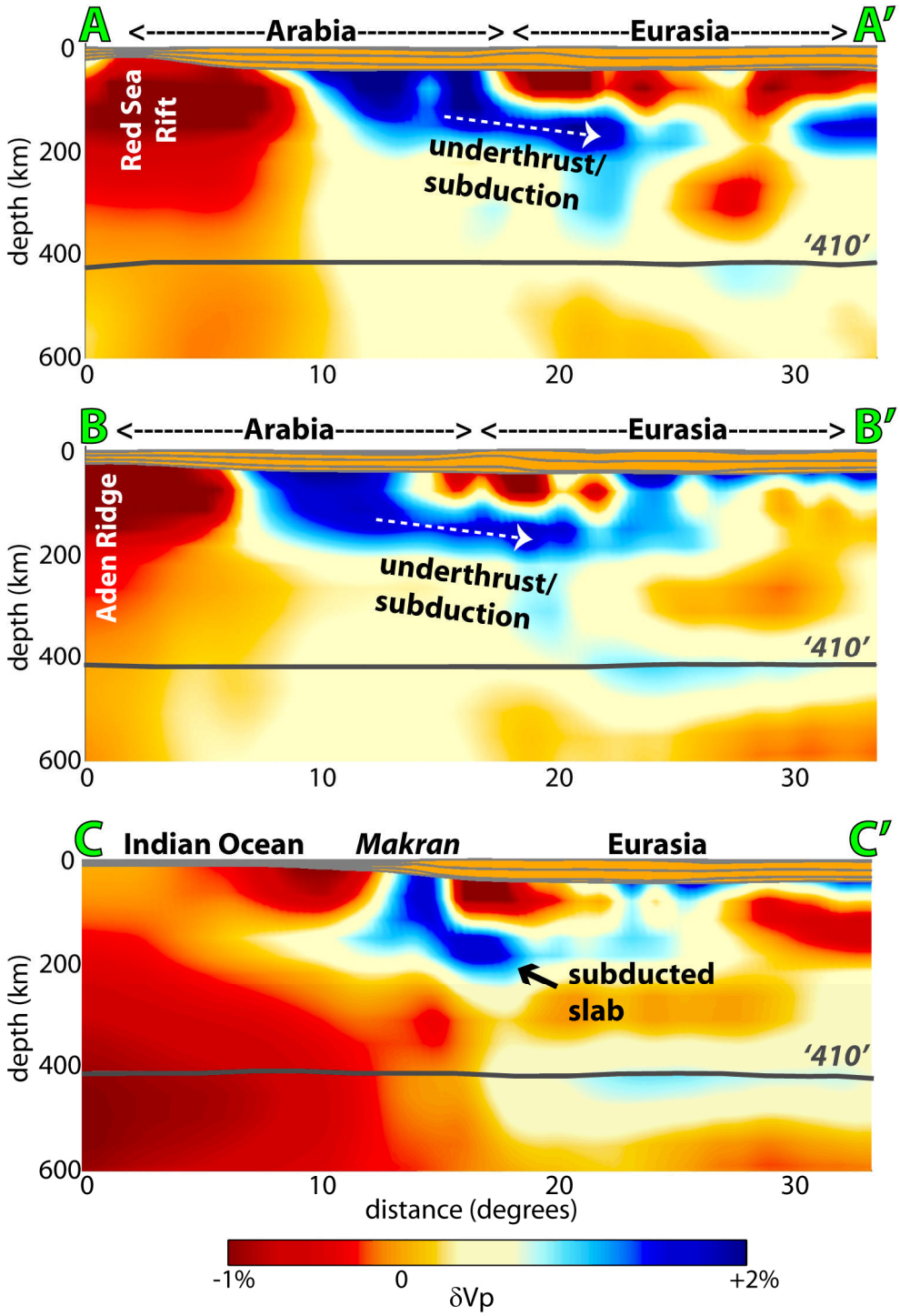
A
<----------Arabia----------> <----------Eurasia----------> A′
Red Sea Rift
underthrust/ subduction
'410'
depth (km)
0
200
400
600
0
10
20
30
B
<----------Arabia----------> <----------Eurasia----------> B′
Aden Ridge
underthrust/ subduction
'410'
C
Indian Ocean
Makran
Eurasia
C′
subducted slab
'410'
distance (degrees)
-1%
0
+2%
δVp

Figure 17

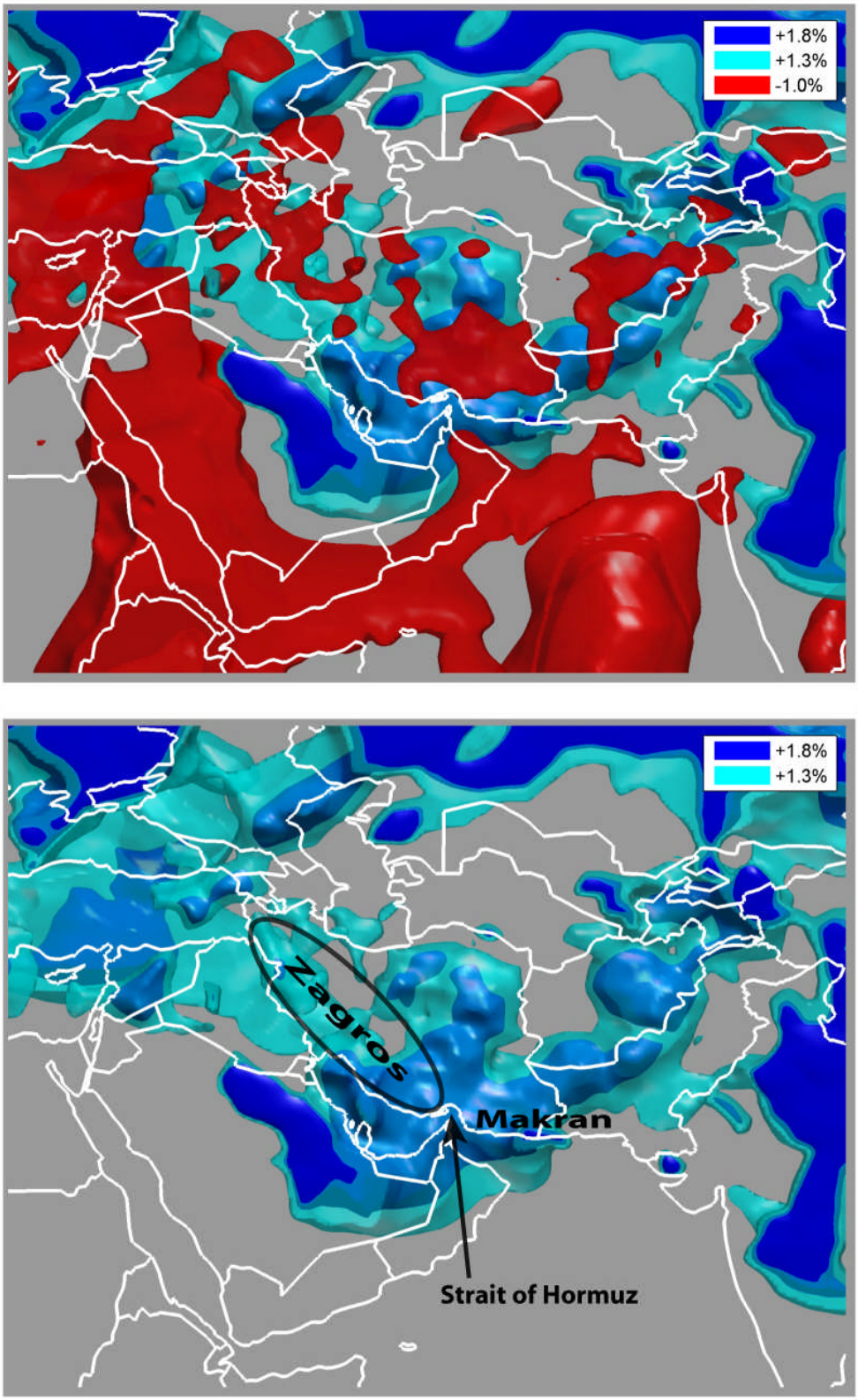

1273
1274 **Figure 18**